Journal of Volcanology and Geothermal Research 423 (2022) 107453

Contents lists available at ScienceDirect

Journal of Volcanology and Geothermal Research

journal homepage: www.elsevier.com/locate/jvolgeores

Assessing hazard and potential impact associated with volcanic ballistic projectiles: The example of La Soufrière de Guadeloupe volcano (Lesser Antilles)

Silvia Massaro [a,b,*], Eduardo Rossi [c], Laura Sandri [a], Costanza Bonadonna [c], Jacopo Selva [a], Roberto Moretti [d,e], Jean-Christophe Komorowski [d]

[a] Istituto Nazionale di Geofisica e Vulcanologia, Sezione di Bologna, Italy
[b] Istituto di Geologia ambientale e Geoingegneria, Consiglio Nazionale delle Ricerche, Roma, Italy
[c] Department of Earth Sciences, University of Geneva, Switzerland
[d] Université de Paris, Institut de Physique du Globe de Paris, UMR CNRS 7154, Paris, France
[e] Observatoire Volcanologique et Sismologique de Guadeloupe, Institut de Physique du Globe de Paris, Gourbeyre, Guadeloupe

ARTICLE INFO

Article history:
Received 22 June 2021
Received in revised form 5 December 2021
Accepted 6 December 2021
Available online 13 December 2021

Keywords:
Probabilistic hazard assessment
Ballistic impact
Risk assessment
La Soufrière de Guadeloupe

ABSTRACT

The fallout of ballistic blocks and bombs ejected from eruptive vents has the potential to produce severe injuries to people and damage to infrastructure in areas proximal to volcanoes. The dimensions and dispersions of ballistic ejecta from explosive eruptions are pivotal parameters to forecast the potential impact associated with future eruptions based on the compilation of probabilistic hazard maps.

In this study, we propose a new probabilistic hazard quantification strategy to provide the probability of Volcanic Ballistic Projectiles (VBPs) to exceed some critical kinetic energy thresholds, considering a variability on the site of the eruptive vents and the effect of wind. La Soufrière de Guadeloupe (Lesser Antilles) is chosen as a test case, focussing on the most likely explosive scenario associated with the eruption of an active lava dome (including phreatic, Vulcanian and Strombolian eruptions). Sensitivity analyses have guided the optimization of input parameters to balance the results stability and computational costs, showing that the topography is a pivotal factor when accounting for the spatial uncertainty on vent locations in the proximity of the dome area. Given an eruption within the adopted scenario, we provide maps showing the probability to exceed different energy reference thresholds for roof's perforation if at least one VBP falls in a target area. These maps are then combined with exposed elements to produce a qualitative exposure-based risk map. We compute the overall probability, conditional on the selected scenario, for roof perforation in a given area when a VBP is ejected. Results show probabilities varying from ca. 2% up to 40% within a few km from the volcano, quickly dropping away from the dome. However, when the probability to exceed the energy reference threshold is only conditional on falling of VBPs in a target area, most of Basse-Terre island would be affected by the 20–60% probability of roof perforation. This work confirms how the choice of a probabilistic approach is key to estimate the likelihood of occurrence of VBPs impacts as a first step towards the development and implementation of pro–active risk reduction strategies in volcanic areas.

1. Introduction

Volcanic eruptions can be associated with a variety of hazardous phenomena, such as tephra dispersal and fallout, pyroclastic density currents, lava flows, gas emissions, debris avalanches, and lahars (e.g., Blong, 1984). The possible impacts associated with all these hazards mostly depend on the characteristics of the eruption and the distance from the vent (e.g., Blong, 2000; Manville et al., 2009; Selva et al., 2010; Jenkins et al., 2015). Tephra dispersal and sedimentation represent one of the main primary hazards associated with explosive eruptions with the potential to impact human life, various economic sectors and the ecosystem (e.g., Wilson et al., 2014: 2017; Jenkins et al., 2015; Bonadonna et al., 2021). Tephra is typically dispersed from the buoyant plume and the umbrella cloud depending on the associated size, density and shape, with lapilli (diameter between 2 and 64 mm) mostly falling from the buoyant plume within tens of kilometres from the vent and volcanic ash (diameter < 2 mm) travelling

* Corresponding author at: Istituto Nazionale di Geofisica e Vulcanologia, Sezione di Bologna, Italy.
E-mail addresses: silvia.massaro@ingv.it, silvia.massaro@igag.cnr.it (S. Massaro), Eduardo.Rossi@unige.ch (E. Rossi), laura.sandri@ingv.it (L. Sandri), costanza.bonadonna@unige.ch (C. Bonadonna), jacopo.selva@ingv.it (J. Selva), moretti@ipgp.fr (R. Moretti), komorow@ipgp.fr (J.-C. Komorowski).

https://doi.org/10.1016/j.jvolgeores.2021.107453

for hundreds to thousands of kilometres, draping the landscape. In addition, blocks and bombs (diameter > 64 mm) can either sediment from the plume margins or follow ballistic trajectories directly from the vent (e.g., Osman et al., 2019). Blocks and bombs represent a major hazard for human life and infrastructures within a few kilometres from the source (e.g., Booth, 1979; Blong, 1984; Wardman et al., 2012; Fitzgerald et al., 2017; Williams et al., 2017; Osman et al., 2019).

In the last decades, tephra hazard assessment has largely focused on ash and lapilli dispersal and fallout because of the potentially large area that could be affected in relation to structural collapse of buildings (e.g., Blong, 1984; Tilling, 1989; Spence et al., 2005; Jenkins et al., 2015), potential disruption of viability on escape routes, damage of power lines and impact on water resources and farming (e.g., Spence et al., 2005; Sword-Daniels, 2011; Wilson et al., 2012; Sulpizio et al., 2014; Loughlin et al., 2015), and impact on airline traffic (e.g., Casadevall, 1994; Folch and Sulpizio, 2010; Biass et al., 2014; Scaini et al., 2014).

Ballistic ejecta (hereafter named Volcanic Ballistic Projectiles, VBPs) have the potential to impact significantly smaller areas with respect to ash and lapilli; nonetheless, VBPs represent a very frequent hazard as they are associated with almost all the typologies of explosive events, from phreatic explosions to Plinian eruptions. Various aspects of ballistic hazard have been analysed including field and experimental observations (e.g., Blong, 1981; Costa et al., 2009; Dellino et al., 2011; Biass et al., 2014, 2016; Fitzgerald et al., 2014; Tsunematsu et al., 2016; Williams et al., 2017; Taddeucci et al., 2017).

The impact of VBPs in terms of roof's perforation has been typically related to the kinetic energy [J], taking into account the size and density of the dense blocks (e.g., Spence et al., 2005; Dellino et al., 2011; Biass et al., 2016; Williams et al., 2017). In general, the impact of a given VBP is mostly a function of size, mass, ejection speed, ejection angle and atmospheric characteristics including wind speed and direction. A large natural variability is expected for all these parameters; this variability needs to be considered in a comprehensive hazard assessment of VBPs. This may be achieved using a Probabilistic Volcanic Hazard Assessment approach (PVHA; e.g., Sobradelo and Martí, 2010; Jenkins et al., 2012; Del Negro et al., 2013; Sandri et al., 2014; Connor et al., 2015; Mead and Magill, 2017), which relies on the simulation of a large number of events by using a range of statistically representative Eruption Source Parameters (ESPs) in order to create a representative framework of the potential hazard. To guide the selection and the definition of the variability for each parameter, sensitivity studies are typically performed (e.g., Tierz et al., 2016; Selva et al., 2018). In quantifying the hazard posed by VBPs, the ESPs (i.e., density, diameter, exit velocity and ejection angle of VBPs) are generally expressed by Gaussian distributions centred on the mean, that can be regarded as a best-guess value (μ), and expressing the uncertainty using the standard deviation (σ) (e.g., Biass et al., 2016).

This study proposes a new probabilistic hazard assessment strategy based on the model of Biass et al. (2016) and aimed at investigating the probability of VBP impact to exceed critical kinetic energy thresholds that can cause significant damage and injuries in a selected area.

We have selected La Soufrière de Guadeloupe volcano (Lesser Antilles; Figs. 1a-b) as case study, focussing on a single eruptive scenario amongst those elaborated by the civil authorities in collaboration with the Observatoire Volcanologique et Sismologique de Guadeloupe (OVSG-IPGP) and listed in the emergency plan for volcanic phenomena that was adopted by the Préfet de Guadeloupe (*Dispositions Spècifiques ORSEC de La Guadeloupe: phènomènes volcaniques,* 2018), which includes phreatic,Vulcanian and Strombolian style eruptions occurred during the last 9 ka (Hincks et al., 2014; Table 1).

La Soufriere de Guadeloupe is currently the second most active volcano in the Lesser Antilles island arc, after Soufrière Hills in Montserrat, and it experienced eruptions with different eruptive styles in the past (e.g., Feuillard et al., 1983; Komorowski, 2005; Komorowski et al., 2008; Legendre, 2012). A parallel study has been carried out in the context of the European Union's Horizon 2020 EUROVOLC Project to investigate the hazard associated with gas emissions at the same volcano (Massaro et al., 2021).

In the first part of this study we briefly show the test volcano and the scenario investigated. Thereafter, we describe the numerical model and the approach used to calculate the probability distribution of the VBP impact energy. In particular, we compare the model with existing data to check its calibration, and we provide a range of sensitivity tests aimed at assessing the best compromise between the reliability of results and computational costs, in relation to the grid resolution and the number of simulated VBPs. We also test the influence of wind on model outputs. As main results, we present the generated probability maps, which take into account the spatial uncertainty associated with the vent opening from the dome area. Finally, we combine hazard and exposed elements to produce a qualitative exposure-based risk map.

2. The case study: La Soufrière de Guadeloupe

2.1. Eruptive history

La Soufrière de Guadeloupe (hereafter indicated as La Soufrière) is an active explosive volcano formed during the last 0.2 *Ma* (Boudon et al., 1988) in the southern part of Basse-Terre island, located in the Lesser Antilles arc (Fig. 1a-b). La Soufrière has a homogeneous magma composition mostly represented by medium-K calc-alkaline basaltic-andesites and andesites. The existing lava dome was formed ca. 500 years ago, after eight dome collapses occurring in the last 8500 years (Fig. 1c) which were caused by blasts of hydrothermal fluids expanding laterally at estimated speeds of 100–230 m s^{-1} (Le Gonidec et al., 2019). The historical eruptive activity has been characterised by persistent hydrothermal events (fumaroles, solfataras, hot springs; Boichu et al., 2011; Ruzié et al., 2012; Gaudin et al., 2013; Villemant et al., 2014; Allard et al., 2014; Brothelande et al., 2014; Gaudin et al., 2016; Tamburello et al., 2019) leading to intermittent phreatic eruptions (Moretti et al., 2020 and references therein).

Despite of numerous debates, the last phreatic eruption that occurred in 1976–1977 has been interpreted as a failed magmatic eruption (Villemant et al., 2005; Boichu et al., 2008, 2011; Ruzié et al., 2012) relating to a small andesitic magma batch stopped its ascent at ca. 3 km below the surface. Notably, this eruption is similar to the 2012 Te Maari eruption, Tongariro, New Zealand (Pardo et al., 2014; Breard et al., 2014). During 1991 degassing decreased before increasing again in 1992. Later, in 2014, a new active region appeared on the summit dome, likely due to new flow paths rearrangement caused by the progressive hydrothermal sealing of fractures. Moreover, the interplay between the hot fluids coming from the magma feeding system and the groundwater fed by the tropical rainfall regime favoured the birth of many thermal springs and fumaroles on the summit dome with intermittent or permanent activity (Komorowski, 2005; Fig. 1c).

2.2. Eruptive scenarios

VBPs represent one of the most significant hazardous phenomena associated with the eruptive activity at La Soufrière, which shows a variety of eruptive styles, including phreatic, Vulcanian, Strombolian and sub-Plinian eruptions (Hincks et al., 2014; Table 1). For the purpose of this study, we focus on phreatic, Vulcanian and Strombolian style eruptions, since the sub-Plinian scenario has already been investigated by Komorowski et al. (2008).

Phreatic eruptions take place in case of the driving fluid is the steam derived from the heated groundwater and show the absence of juvenile material (e.g., Rosi et al., 2018 and references therein).

These eruptions cause sudden eruptive phenomena (i.e., ash-venting, ejection of ballistics and dense mixed ash-and-vapor clouds) with limited or absent premonitory signs to new explosive phases. This is because they are triggered by the injection of fluids and heat of

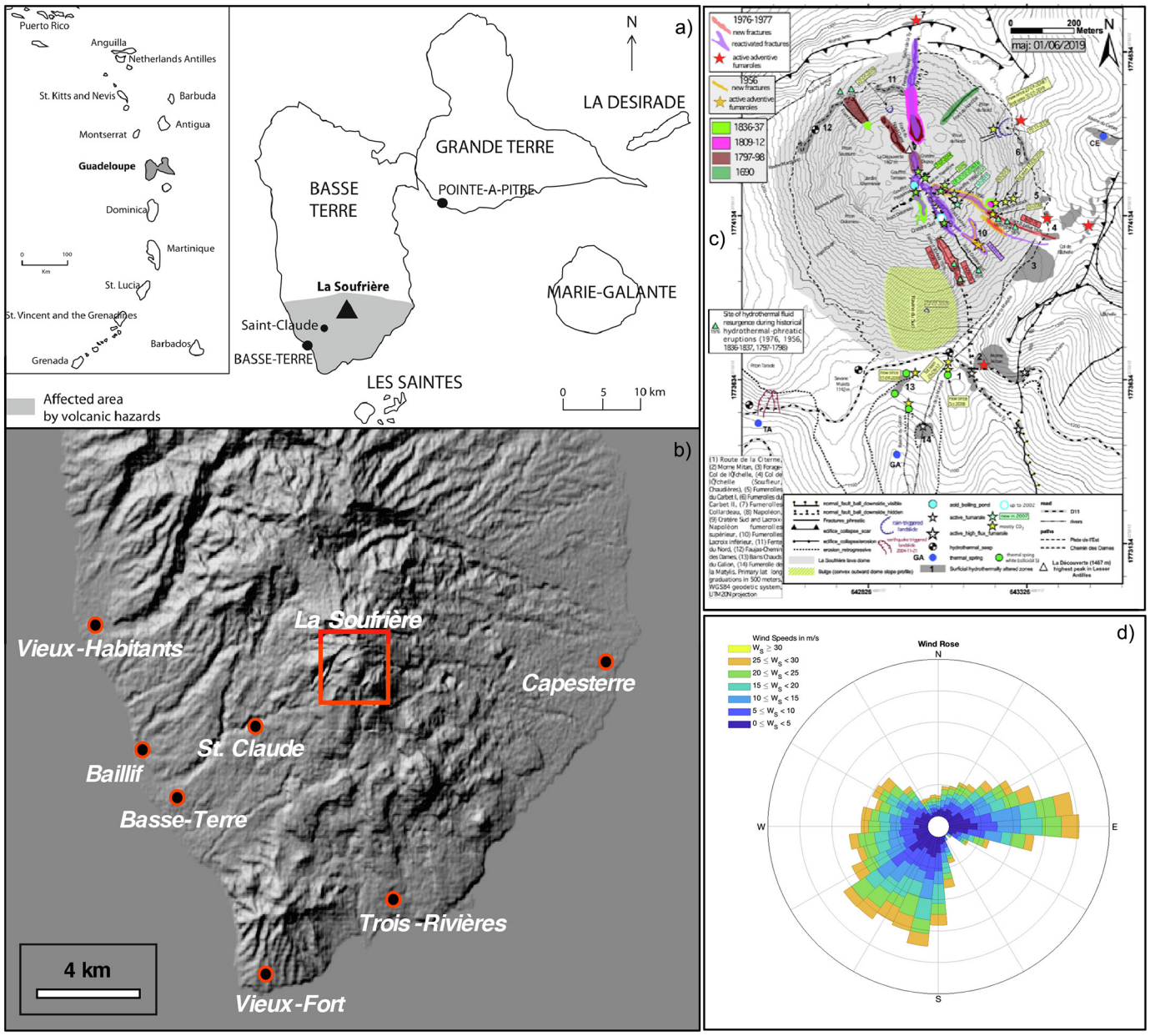

Fig. 1. a) Map of Guadeloupe showing the active volcano La Soufrière, and the major towns (St. Claude, Basse-Terre, Pointe-a-Pitre). Inset map showing the location of Guadeloupe in the Antilles region (modified from Chenet et al., 2014). b) Digital Elevation Model (DEM) of the computational domain, including the southern part of the Basse-Terre island. The main urban centres are indicated with black-red dots. The DEM resolution is set to 10 m; c) Location map of the main structures, historical eruptive vents, observed fumarolic activity on La Soufrière lava dome (modified from the OVSG-IPGP report, October 2018); d) Windrose diagram showing the daily wind conditions at La Soufrière during 2017–2018 from the "Piton Sanner" meteorological station located on the top of the dome.

magmatic origin into the aquifers and/or hydrothermal system, which becomes overpressurized (Moretti et al., 2020 and reference therein).

Vulcanian eruptions may be associated with a wide range of magnitudes, depending on how much the upper feeding system of the volcano is emptied during transient eruptive phases. They are usually repetitive in time, and can last from months to several years (i.e., Vulcano island 1888–1890 eruption, Mercalli and Silvestri, 1891; Di Traglia et al., 2013; Selva et al., 2020; Montserrat, 1995–2005, Druitt et al., 2002). Associated main primary volcanic hazards include ballistic ejection and tephra sedimentation.

Strombolian eruptions are associated with smaller magnitudes with respect to the Vulcanian ones. Their duration spans from short-lived to persistent activity (i.e., Stromboli volcano). Eruptive dynamics is dominated by small eruptive columns that deposit loose or welded scoria in the proximity of the source. Also, in this case, associated main primary volcanic hazards are ballistic ejection and tephra sedimentation even though characterised by a significantly smaller extension of impact with respect to Vulcanian eruptions.

At La Soufrière, phreatic eruptions have been recurrent (e.g., Komorowski, 2005; Hincks et al., 2014; Moretti et al., 2020) and short-lived, even though some events posed significant disruption with partial evacuations for an extended period (Komorowski, 2005). Vulcanian and Strombolian eruptions also occurred in the historical activity of La Soufrière, even if less frequently with respect to phreatic eruptions (Hincks et al., 2014; Table 1).

For the sake of simplicity, in this study VBPs associated with a single averaged scenario of explosive eruptive style derived from phreatic, Vulcanian and Strombolian eruptions. In Table 2 we provide the ESPs

Table 1
Main events occurred at La Soufrière de Guadeloupe classified as: non-magmatic, non-explosive edifice collapses (E); magmatic explosive (M); phreatic events (P), or failed magmatic (F), as in 1976. A question mark indicates the eruption date is uncertain. The last confirmed major magmatic eruption of La Soufrière de Guadeloupe was 1530 CE (CE: Common Era; from Hincks et al., 2014).

Start date	Type	Description
6535 BCE	E	Edifice collapse - not magmatic, not explosive
4000 BCE?	M	VEI 2 explosive Strombolian
3600 BCE?	M	VEI 2 explosive Vulcanian
3360 BCE	M	VEI 3 magmatic dome eruption, possibly explosive
2400 BCE?	E	Edifice collapse - not magmatic, not explosive
1625 BCE	M	VEI 3–4 explosive magmatic with edifice collapse and blast (possible cryptodome?)
1400 BCE	M	VEI 3–4 explosive magmatic with edifice collapse and blast (cryptodome)
1065 BCE?	E	Edifice collapse - not magmatic, not explosive
980 BCE	M	VEI 3 magmatic dome eruption, possibly explosive
465 BCE	M	VEI 3 explosive magmatic dome eruption with edifice collapse and blast
310 CE	M	VEI 2 explosive Strombolian
605 CE	E	Edifice collapse - not magmatic, not explosive
1530 CE	M	VEI 2–3 explosive Subplinian and dome magmatic eruption with edifice collapse
1635 CE?	M	VEI 2 explosive magmatic, possibly Vulcanian
1690 CE	P	VEI 1 Phreatic - not magmatic but explosive (Komorowski, 2005)
1797 CE	P	VEI 1 Phreatic - not magmatic but explosive (Komorowski, 2005)
1812 CE	P	VEI 1 Phreatic - not magmatic but explosive (Komorowski, 2005)
1836 CE	P	VEI 1 Phreatic - not magmatic but explosive (Komorowski, 2005)
1956 CE	P	VEI 1 Phreatic - not magmatic but explosive (Komorowski, 2005)
1976 CE	F	VEI 1 failed (still-born) magmatic explosive (Komorowski, 2005)

(in particular exit velocity, diameter and density of ballistic blocks) related to the adopted eruptive scenario, taken from the representative initial conditions of phreatic, Vulcanian and Strombolian eruptions available in the literature. A detailed description of these parameters is reported in Appendix A.

3. Methods

3.1. Numerical model

GBF is implemented for the computation of hazard assessments of VBPs (Biass et al., 2016). It is based on the general numerical solution of the momentum equations, with gravity and air drag as the main forces acting on the object. The model takes into account the presence of a standard atmosphere, the influence of a constant wind along the vertical profile and a region of reduced drag in the proximity of the vent (Mastin, 2001). Every particle is assumed to be a sphere having a mass m, an average diameter D, a position r and a velocity $\boldsymbol{v}$, calculated considering an inertial frame of reference on the ground. The VBP trajectory is described as follows:

$$\boldsymbol{u} = \boldsymbol{v} - \boldsymbol{w} \tag{1}$$

$$\ddot{r} = \dot{\boldsymbol{v}} = \frac{-u\,|u|\,A\,\rho_a C_d}{2m} + \boldsymbol{g} \tag{2}$$

where A is the clast cross area, $\boldsymbol{u}$ the velocity of the VBP relative to the wind $\boldsymbol{w}$, $\boldsymbol{g}$ the acceleration gravity vector, C_d the drag coefficient and ρ_a the air density. C_d does depend on the altitude, velocity, shape, orientation, and roughness of the VBPs (e.g., Tsunematsu et al., 2016), while ρ_a only depends on the altitude. According to Biass et al. (2016), C_d is calculated through the particle Reynolds number which depends on the air characteristics and the diameter and speed of the VBPs.

The GBF assumes $C_d \approx 0.1$–0.5, with a reduced drag for distances smaller than the reduced drag radius. The reduced drag is justified under the assumption that at the beginning of the explosion, clasts are ejected together with an expanding mass of gas. This results in a reduction of the effective drag around the object.

C_d is calculated through the particle Reynolds number which depends on the air characteristics and the VBP diameter and speed. C_d is set to 0.1 if Re is $<3 \times 10^5$, otherwise is set to 0.5. Since VBPs are ejected together with an expanding mass of gas, C_d may be reduced following Eq. (9) in Biass et al., 2016.

One of the main advantages of GBF relies on the capability of modelling a large number of VBPs in a short computational time. This aspect makes GBF suitable for a probabilistic investigation of VBP trajectories, impact energies and distances reached by VBPs. The initial conditions for each VBP are sampled stochastically from a Gaussian distribution on each input parameter (i.e., exit velocity, particle density and size, and ejection angles). The distribution of VBP size is assumed to be Gaussian in the Krumbein scale (also called the *phi scale*), resulting in a log-normal distribution on a linear scale on the size. It is also assumed that each VBP has a spherical shape: consequently, the mass can be immediately calculated from the diameter and the density (Biass et al., 2016).

It is important to stress that the assumed VBP size distribution affects the results of simulations because the VBP impact energy is fundamentally controlled by their size, mass and altitude. For this reason, in Figs. 2d-e-f we provide the correlation between impact energy and diameter of the simulated VBPs. For each number of ejected clasts (10^5, 10^6, 10^7) we observe an exponential increase of the impact energy at increasing the diameter. Obviously, the VBP distribution is not known a priori, but the uncertainties associated with the chosen size distribution need to be taken into account for quantifying the epistemic uncertainty in hazard assessment (even if it is out of the scope of this paper).

In our study, the simulated VBP locations obtained from a forward use of GBF are compared with the observed data from La Soufrière (Section 4.1). The procedure implemented to assess quantitatively the probabilistic hazard differs from the one proposed by Biass et al. (2016) as ours it is based on the independent evaluation of the probability of exceeding a given energy threshold and the probability of having clast fallout of a given size per cell (Section 4.2). This results in an alternative version of the post-processing routine which has been specifically coded in MATLAB for the purposes of this paper (see Supplementary Material).

In Biass et al. (2016), the probability P to exceed a given energy threshold E_t in the cell A_{ij}, conditional to clast ejection, is quantified as:

Table 2
Eruption Source Parameters (ESPs) used in the sensitivity analysis. Density, diameter and exit velocity of the clasts are expressed as Gaussian distributions with mean and standard deviation. These values are the averages of the source parameters taken from the reference eruptions (Tsunematsu et al., 2016; Kilgour et al., 2010; Rosi et al., 2018; Fagents and Wilson, 1993; Druitt et al., 2002; Clarke et al., 2002; Formenti et al., 2003; de Michieli Vitturi et al., 2010; Alatorre-Ibargüengoitia et al., 2012; Vanderkluysen et al., 2012; Maeno et al., 2013; Biass et al., 2016; Houghton et al., 2017; Appendix A).

		Unit	μ	σ
Source	Density	kg m^{-3}	2500	100
	Diameter	m	0.55	0.45
	Exit velocity	m s^{-1}	90	60
	Tilt angle	deg	0	
	Spread angle	deg	90	
Wind	Speed	m s^{-1}	0	
	Direction	deg	0	
Drag	Pressure	hPa	1.01×10^5	
	Temp at sea level	K	298	
	Thermal lapse	°C km^{-1}	-6.50×10^{-3}	
	Reduced Drag radius	m	200	

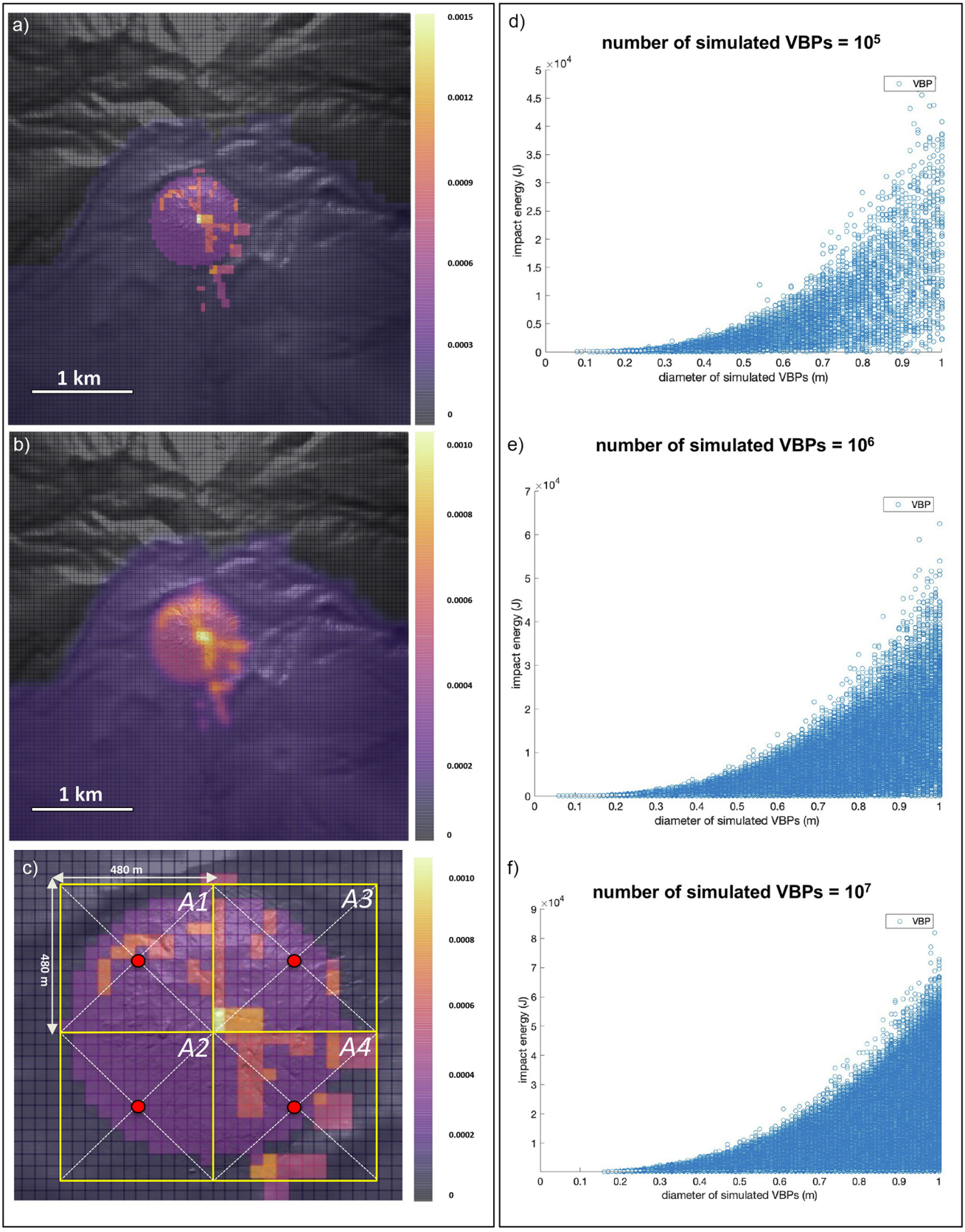

Fig. 2. a) Best-guess probability map of vent opening; b) Gaussian filter with $\sigma = 40$ m applied to consider the spatial uncertainty of the data and to avoid a scattered spatial distribution due to the limited sampling; c) Magnification of the spatial map displaying the probability of vent opening within four regular macroareas (*A1*, *A2*, *A3*, *A4*). The corresponding vents are located in the centre of each macroarea (red dots; *A1:* 643451 E, 1774608 N, altitude: 1344 m; *A2:* 643451 E, 1774316 N, altitude: 1273 m; *A3*: 643820 E, 1774748 N; altitude: 1426 m; *A4*: 643820 E, 1774316 N; altitude:1345 m). Plots of the VBPs diameter vs impact energy are shown in: d) fixed VBPs $= 10^5$; e) fixed VBPs $= 10^6$; f) fixed VBPs $= 10^7$. The diameter of the simulated clasts ranges between −9.89 1.66 ϕ.

$$P_{(A_{ij},E_t)=}\frac{\sum_{i,j} n_{A_{ij},E_t}}{n_{VBP}} \quad (3)$$

where n_{A_{ij},E_t} is the number of simulated VBPs falling into the cell A_{ij} overcoming E_t, and n_{VBP} is the total number of simulated VBPs.

In this study, the symbology to express the probability is indicated with θ. In particular, we split in two factors the probability shown in eq. (3), recalling it as θ^e:

$$\theta^e{}_{(A_{ij},E_t)=}\frac{\sum_{i,j} n_{A_{ij},E_t}}{n_{VBP,A_{ij}}} * \frac{n_{VBP,A_{ij}}}{n_{VBP}} = \theta^{ec}{}_{(A_{ij},E_t)} * \theta^f{}_{A_{ij}} \quad (4)$$

where $\theta^{ec}{}_{(A_{ij},E_t)}$ defines the conditional probability to exceed a given threshold E_t when a VBP falls in the cell A_{ij} (i.e., $n_{VBP,Aij}$), and $\theta^f{}_{A_{ij}}$ is the probability that a clast reaches that cell.

As energy reference thresholds, we consider the median values of the fragility function for residential buildings provided by Williams et al. (2017) and suited for the timber weatherboard, sheet material and reinforced concrete (Table 3), the most frequent materials for roof types existing in Guadeloupe (Spence et al., 2008).

3.2. Probability of vent opening

The spatial probability of vent opening for future explosive explosions is a very important aspect to take into account when the hazard assessment is quantified. In our case, this probability is derived on the base of existing literature data on the main geological structures, historical eruptive vents, past observed fumarolic activity and measurements of the present-day gas emission rates (Gaudin et al., 2013; Allard et al., 2014; Brothelande et al., 2014; Gaudin et al., 2016; OVSG-IPGP reports, 2018; Fig. 1c).

In this paper, we follow the approach by Selva et al. (2012) that considers indicators of the susceptibility to vent opening, ranking them in terms of importance and considering potential uncertainty on data. According to this approach, we quantify the conditional probability of vent opening, given an explosive event, in the generic k-th cell out of all possible cells (N) into which the volcanic domain was divided. In our case we design a domain grid of 98 × 98 cells, thus $N = 9604$, and the cell spacing is about 40 m (Fig. 2a).

To each k^{th} cell, we assign a total score ω_k which equals the sum of five scores on the following features:

i. a score of 1 if the k^{th} cell is inside the domain but outside the dome
ii. a score of 2 if the k^{th} cell is inside the domain and inside the dome
iii. a score of 3 if in the k^{th} cell there are main geological structures (fractures and faults)
iv. a score of 4 if in the k^{th} cell there have been past observed fumaroles
v. a score of 5 if in the k^{th} cell there is present-day fumarolic activity and/or significant gas fluxes.

This is a simple and preliminary approach; nonetheless, it represents the simplest approach allowing to embed current views on where a vent is more likely to open based on up-to-date indicators of potential future phreatic activity. We assume that the best guess probability of vent opening (θ^k) in k-th cell is proportional to its total score ω_k, and that the cells in the domain represent a set of complete and mutually exclusive potential vent positions ($\sum_{k=1}^{N}\theta^k = 1$). Therefore, the probabilities θ^k ($k = 1, \ldots, N$) can be written as:

$$\theta^k = \frac{\omega_k}{\sum_{j=1}^{N}\omega_j} \quad (5)$$

To take into account the spatial uncertainty of the data and to avoid a scattered spatial distribution due to the limited sampling, we apply a Gaussian filter with $\sigma = 40$ m (Fig. 2b). This value is related to the maximum error on the position of the different data used to derive the map.

Table 3
Energy thresholds (E_t) representing the median values for fragility functions for timber weatherboard (E_{t_1}), sheet material (E_{t_2}) and reinforced concrete (E_{t_3}). These values are referred to the maximum damage state (Williams et al., 2017).

Fragility function suite	*Et [J]*
Timber weatherboard	360
Sheet material	650
Reinforced concrete	2750

3.3. Exceedance probability accounting for vent position uncertainty

In this section we describe the approach used to calculate the probability to exceed the energy thresholds E_{tm} ($m = 1,2,3$) that are relevant for roof perforations at La Soufrière (Williams et al., 2017; Table 3). For the sake of clarity, we provide a flowchart of the model design in Fig. 3 showing each step of the following procedure. Recalling eq. (4), both the probabilities $\theta^e{}_{(A_{ij},E_t)}$ and $\theta^{ec}{}_{(A_{ij},E_t)}$ are investigated.

To fully explore the uncertainty on vent position, a large amount of VBPs should be ejected from each k^{th} cell defined in the previous section. However, given our computational resources, this is too expensive in terms of computational time. To reach a balance between computational feasibility and accuracy, we first focus on the dome area which is the most likely zone for phreatic events in the future, due to past eruptive vent locations and the on-going degassing activity. Thereafter, we identify four macroareas of equal size (480 m × 480 m) covering the dome (*A1, A2, A3, A4*; Fig. 2c). The vent opening probability associated to each j-th macroarea ($\omega_j, j = 1, \ldots 4$) is the sum of the probabilities of vent opening θ^k (eq. 5) of the N_j cells of the finer vent-grid belonging to that macroarea, that is:

$$\omega_j = \sum_{k=1}^{N_j}\theta^k \quad (6)$$

In this work, we assume that the location of the next eruptive event for the adopted scenario will be on the dome (Fig. 2c), and thus such probabilities should be normalized to this area:

$$\omega\prime_k = \frac{\omega_k}{\sum_{j=1}^{4}\omega_j} \quad (7)$$

for $k = 1, \ldots 4$.

We run GBF launching a large (but tractable) number of VBPs (see Section 4.1 for details on such number) from the centres of the four macroareas on the dome (Fig. 2c), assuming that these simulations are representative of the whole macroarea. Under these assumptions and considering the total probability theorem, the probability $\theta^f{}_{A_{ij}}$ that a clast reaches that cell and the probabilities $\theta^{ec}{}_{A_{ij},m}$ and $\theta^e{}_{A_{ij},m}$ to exceed $E_{tm}(m = 1,2,3)$, conditional on the ejection of a clast during an eruption within the adopted scenario and from any vent within the dome area, can be computed as:

$$\theta^f{}_{A_{ij}} = \sum_{k=1}^{k=4}\omega'_k\left[\theta^f{}_{A_{ij,k}}\right] = \sum_{k=1}^{k=4}\omega'_k\left[\frac{n_{VBP,A_{ij,k}}}{n_{VBP}}\right] \quad (8)$$

$$\theta^{ec}{}_{A_{ij},m} = \sum_{k=1}^{k=4}\omega'_k\left[\theta^{ec}{}_{A_{ij},E_{tm},k}\right] \quad (9)$$

and

$$\theta^e{}_{A_{ij},m} = \sum_k \omega'_k\,\theta^e{}_{A_{ij},E_{tm},k} = \sum_k \omega'_k\left[\theta^{ec}{}_{A_{ij},E_{tm},k*}\theta^f{}_{A_{ij,k}}\right] \quad (10)$$

where we use the same notation as in eq. (4), adding an index k to the summands to highlight the contribution to the final probability given

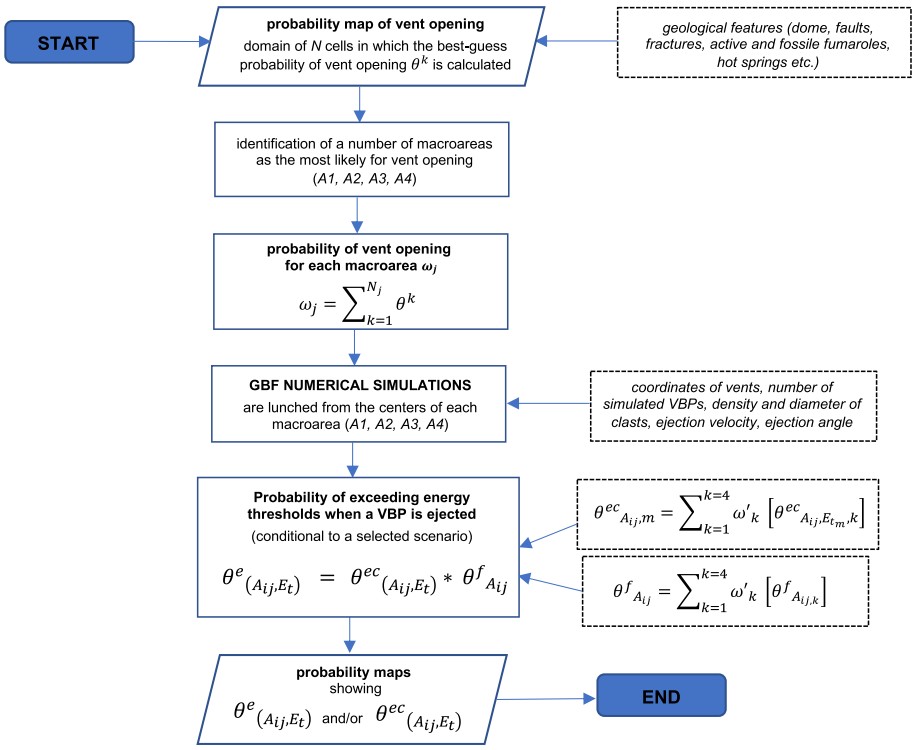

Fig. 3. Flowchart of the logical process describing how to calculate the overall exceedance probability accounting for the vent position uncertainty.

by the simulations from each of the four different macroareas. It is important to stress that eq. (9) defines the conditional probability to exceed a given energy threshold E_t when a VBP falls in the cell A_{ij}, while eq. (10) defines the probability that a clast reaches the cell $A_{ij}$and that its impact energy exceeds the given threshold E_t, in all cases summing the contribution of all macroareas. In Appendix B, we show further simulations carried out from the centres of six peripheral irregular macroareas around the dome.

As the peripheral macroareas are very large, we do not deem the simulations from their centers as representative for the whole macroarea. For this reason, we do not include the results of these simulations in the probability maps: we think this would need to run many more simulations, beyond our computational capability, from other locations inside these macroareas (not only from their centers).

4. Comparison with field data and sensitivity analyses

4.1. Comparison between model results and field observations at La Soufrière

Although La Soufrière experienced different eruptive styles (see Table 1), phreatic eruptions represent the most frequent eruptive phenomena based on the historical record (occurred in 1690; 1798–98; 1812; 1836–37; 1956 and 1976–77) and on an extrapolation over the last 15 kyr for which other eruption type return rates have been determined (Komorowski, 2005).

Phreatic eruptions can be isolated events or precursory activities of magmatic phases (Rosi et al., 2018 and reference therein) which can generate lethal phenomena such as VBPs fallout and pyroclastic density currents (PDCs) (e.g., Sheridan and Malin, 1983; Fitzgerald et al., 2014), as for the 1976–77 crisis case where an injection of magma at depth was invoked as a triggering mechanism (e.g., Ruzié et al., 2012). In particular, the 14th September 1976 blast (Sheridan, 1980; Hincks et al., 2014) showed similarities with the blast phase of the Vulcano's Breccia di Commenda eruption (phase 2a; Rosi et al., 2018), which produced numerous violent explosions with an asymmetric fallout of ballistic blocks during the emplacement of a lithic-rich, blast-like pyroclastic density currents.

In Fig. 4 we provide the available field observations on the distribution of VBPs associated with the 1956 and 1976–77 eruptions

Table 4
a) Ballistic parameters inferred for the 1956 and 1976–77 eruptions (from Komorowski, 2015); b) Eruption Source Parameters (ESPs) used in the GBF simulations carried out to reproduce the observations of the 1956 and 1976–77 eruptions. The simulations eject 10^5 VBPs from a single vent located on the summit dome (643,820 E; 1,774,316 N, UTM coordinate system) in absence of wind. Two maximum clast diameters of 20 cm and 10 cm are fixed, considering a density of ballistics varies between 2500 and 2600 kg m^{-3} (Komorowski et al., 2008), in order to match the maximum mass of the ballistics mapped in the field for 1956 and 1976–77 eruptions, respectively. The exit velocities are in agreement with the source parameters of phreatic eruptions reported in literature (Kilgour et al., 2010; Tsunematsu et al., 2016).

a)

max VBP mass	VBP density DRE	max VBP volume	VBP diameter
kg	*kg m^{-3}*	*m^3*	*cm*
1956-eruption			
10	2600	0.0038	19.44
10	2500	0.004	19.69
1976–77-eruption			
1	2600	0.0004	9.02
1	2500	0.0004	9.14

b)

Source	VBP density	2500–2600	kg m^{-3}
	VBP diameter	0.2–0.1	m
	Ejection velocity	30–150	m s^{-1}
	Tilt angle	0	deg
	Spread angle	90	deg
Drag	Pressure	1.01×10^5	hPa
	Temp at sea level	298	K
	Thermal lapse	-6.50×10^{-3}	°C km^{-1}
	Reduced Drag radius	200	m

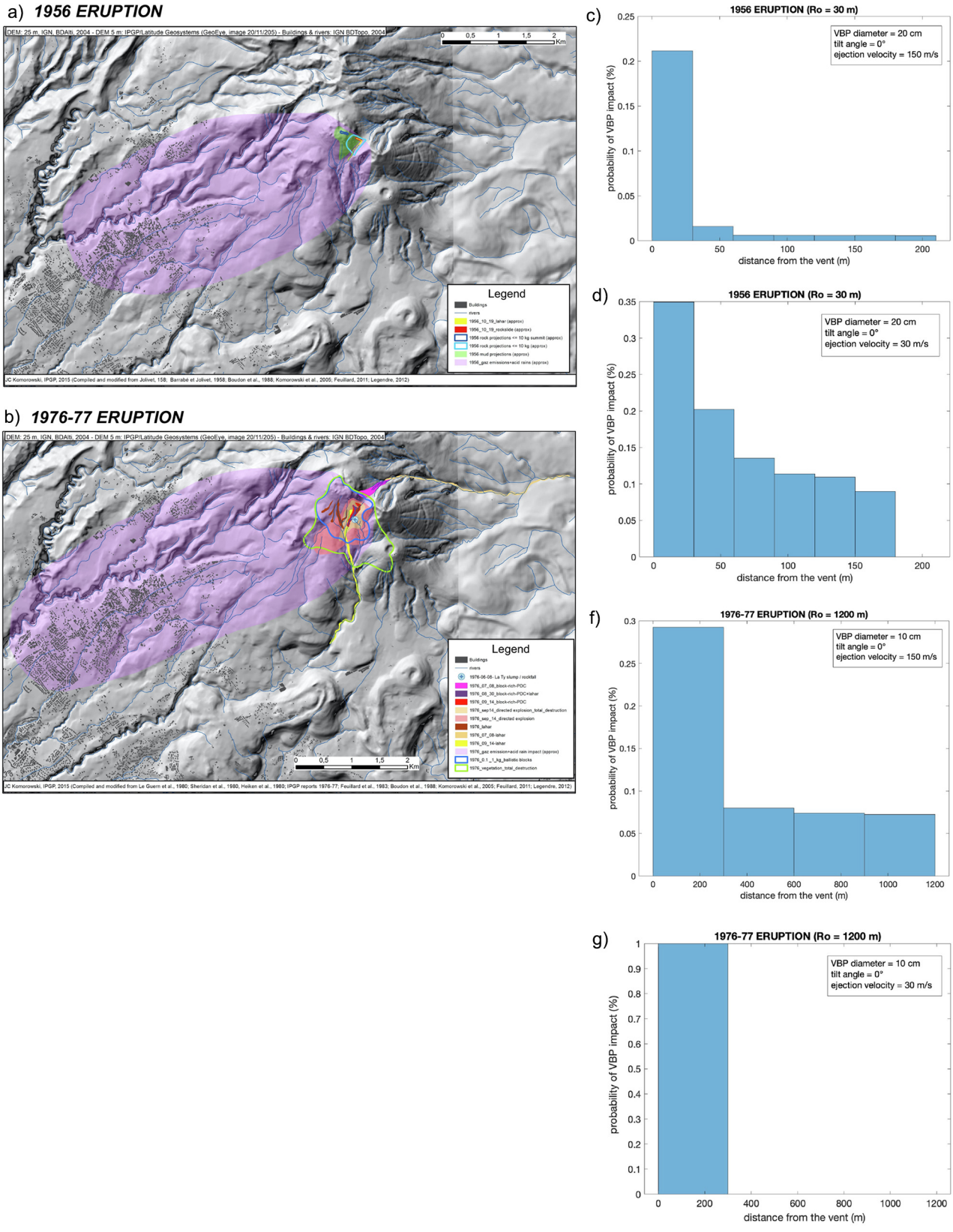

Fig. 4. Maps showing the distribution of various volcanic phenomena (ballistic fallout, pyroclastic density currents, rockfall, lahars, gas emissions) and impacts (i.e., vegetation destruction, acid rains) associated to a) 1956 and b) 1976–77 eruptions at La Soufrière (from Komorowski, 2015). Percentage of VBPs sedimented at varying distance from the vent with respect to the total number of VBPs released (10^5), considering c) a clast diameter of 20 cm, ejected with a tilt angle = 0° at an exit velocity of 150 m s^{-1}; d) a clast diameter of 20 cm, ejected with a tilt angle = 0° at an exit velocity of 30 m s^{-1}; e) a clast diameter of 10 cm, ejected with a tilt angle = 0° at an exit velocity of 150 m s^{-1}; f) a clast diameter of 10 cm, ejected with a tilt angle = 0° at an exit velocity of 30 m s^{-1}(see Table 4a). *Ro* represents the maximum radial distance of the observed ballistic clasts (from Komorowski, 2015).

(Komorowski, 2015). In the case of the 1956 eruption, two ballistic fields have been identified at the summit dome (dark blue contour; Fig. 4a) and along the South-Eastern flank (light blue contour; Fig. 4a) with a maximum clast mass of 10 kg. For the 1976–77 eruption, the clast mass ranges from 0.1 to 1 kg with a wider dispersion angle (dark blue contour; Fig. 4b). For 1956 ballistic fields, we observe that the maximum radial distance reached by ballistic clasts *Ro*, is ca. 30 m. For 1976–77 case, *Ro* is ca. 1200 m. The parameters inferred for 1956 and 1976–77 eruptions are taken from Komorowski (2015) and reported in Table 4 (a).

Field observations of VBPs have been compared with the results from the GBF simulator. For computational efficiency reasons, simulations eject 10^5 VBPs from a single vent located on the summit dome (643,820 E; 1,774,316 N, UTM coordinate system) in absence of wind. Considering the density of ballistics (composed mainly by andesitic juvenile and accidental lithic clasts) varies between 2500 and 2600 kg m^{-3} (Komorowski et al., 2008), we fix two maximum clast diameters of 20 cm and 10 cm, in order to match the maximum mass of the ballistics mapped in the field for 1956 and 1976–77 eruptions, respectively (Table 4a). We set two exit velocities (30 m s^{-1} and 150 m s^{-1}) as the range provided by Mastin (1995) for La Soufrière de Guadaloupe considering the observed data in La Guern et al. (1980). These data are also in agreement with the source parameters of phreatic eruptions reported in literature (Kilgour et al., 2010; Tsunematsu et al., 2016). To compare the model results and the field observations, we use the ESPs shown in Table 4 (b).

In Fig. 4c, we show the frequency histogram of the number of VBPs fallen at different distances from the vent, for the 1956 eruption model. The 21% of the simulated VBPs is included within the maximum observed distance $Ro = 30$ m considering 150 m s^{-1} as ejection velocity. This frequency rises to 35% if we consider 30 m s^{-1} (Fig. 4d). In Figs. 4f-g, the frequency histogram for 1976–77 eruption model is shown by using both 150 and 30 m s^{-1} as ejection velocity. In this case we observe that 100% of the simulated VBPs is within the maximum observed distance $Ro = 1200$ m. We therefore conclude the GBF simulator is able to approximately catch the observed natural dispersal areas of VBPs and thus can be considered suitable for reproducing the ballistic field associated to selected eruptive scenarios (i.e., phreatic). This also makes us confident of the suitability of the GBF for the construction of probabilistic hazard maps for VBPs.

It is important to stress that, even if the observed VBP distribution showed a clear directionality in both eruptions (Figs. 4a-b) as typical at La Soufrière (the vent is on the flanks of the dome, adding a directed lateral component to the ejected blocks), in our modelling the VBP sedimentation is symmetrical with respect to the vent in order to ensure a maximum clast dispersion: the directionality shown in Figs. 4a-b has not been explored here due to lack of data.

4.2. Sensitivity analysis on the number of simulated VBPs

We performed a sensitivity analysis to constrain the minimum number of clasts that are required to have a stable energy distribution in each of the four cells under analysis, here used as a test-area (Fig. 5a). In order to define the Gaussian distributions for the VBP diameter, density and exit velocity, we compute the mean value μ and the standard deviation σ of the corresponding values reported for the above selected eruptions (Section 2.2), given in Table 2. The conditions of a standard atmosphere, no wind and a reduced drag radius of 200 m are used to calculate drag forces (e.g., Mastin, 2001; Biass et al., 2016).

To test the sensitivity to the number of simulated VBPs, we vary such number between 10^5 and 10^8, with multiplicative increment of 10, and test the effect on the four cells (c_1, c_2, c_3, c_4) surrounding the dome, the Hospital Les Nouvelles Eaux-Vives and the centre of *St*. Claude village. The cells are located respectively ca. 500, 2600, 4000 and 5200 m from the vent (Fig. 4a). The grid resolution is set to 260 m × 220 m (corresponding to 100 × 100 cells).

The first step is to verify the existence of a plateau in the impact-energy probability as the number of simulated VBPs increases (from 10^5 to 10^8). In Fig. 5b, we show the impact-energy probability in the four selected cells as a function of the number of simulated VBPs (i.e., number of VBPs fallen in the cell with impact energy above a given threshold divided by the total number of VBPs released).

As expected, results show that, no matter what the number of simulated VBPs is, the number of fallen VBPs in the four cells decreases with distance from the vent. Moreover, when the number of the released VBPs is 10^5, the probability distribution shows scattered frequency peaks, especially in c_3 and c_4. Smaller fluctuations are instead observed when the released VBPs is 10^6. Using a released VBPs number of 10^8 or 10^7 (corresponding to the violet and yellow bins, respectively), a stability in the impact-energy probability can be observed for each cell.

To better highlight the fluctuations observed in each cell, we represent the absolute difference between the exceedance probability for each energy class associated to 10^8, and 10^5, 10^6, 10^7 released VBPs, respectively (Fig. 5c). The probabilities related to $|10^8–10^5|$ (red line) show several spikes for the areas nearest to the vent (cells c_1-c_2). The probabilities related to $|10^8–10^6|$ (blue line) reveal a slightly flattened trend, with scattered spikes only in few bins showing differences less than 0.005% in c_1, 0.015% in c_2, 0.07% in c_3 and 0.35% in c_4 with respect to the probabilities related to $|10^8–10^7|$ (black line). This confirms a marked flat trend in all investigated cells.

This test demonstrates that the normalized energy probability in the cells under analysis stabilizes when the total number of released VBPs is at least 10^7 (black line; Fig. 5c). This implies that any higher number of VBPs (i.e. $> 10^8$) will likely produce the same normalized energy distributions in each cell, but at a higher computational cost.

We conclude that VBPs in the range of 10^7–10^8 VPBs can be reasonably used as a good compromise to produce stable probability energy distributions in each cell that do not depend on the number of total VBPs ejected from the vent. However, simulating a number of 10^7–10^8 VBPs would still imply a considerable computational effort both in terms of cpu and memory space. Therefore, a strategy is needed for the reduction of total VPBs without affecting the final accuracy and precision of the results. This can be obtained by reducing the spatial resolution of the domain and concentrating only on the highest energy levels. Considering the results shown in Fig. 5, we check the stability of exceedance probability of VBPs impact energy for the chosen energy thresholds E_t (Table 2) in each cell, as a function of the released VBPs in every simulation (Fig. 6). In this case, we vary the grid resolution of the domain (260 m × 220 m, 516 m × 445 m, 860 m × 752 m, corresponding respectively to 100 × 100 cells, 50 × 50 cells, 30 × 30 cells) in order to set the best strategy for the compilation of the hazard assessment. As a matter of fact, when using 260 m × 220 m grid resolution (Fig. 6a), releasing less than 10^6 VBPs does not ensure stable probabilities for any of the energy thresholds considered, while releasing more than 10^6 VBPs shows a plateau only for the energy levels corresponding to the timber weatherboard and sheet material (E_t 360 J and 650 J, respectively). Better results can be observed using coarser grid resolutions of 516 m × 445 m (Fig. 6b) and 860 m × 752 m (Fig. 6c), where a stable exceedance probability is achieved when the number of released VBPs is larger than 10^6 for all E_t values.

In the end, to balance computational cost and result stability in relation to impact-energy probability, 2×10^6 clasts is taken as the optimum number of VBPs to be released from the vent in each model run (a simulation is completed in ca. 45 min on Intel i5). This number is twice the one used in Biass et al. (2016).

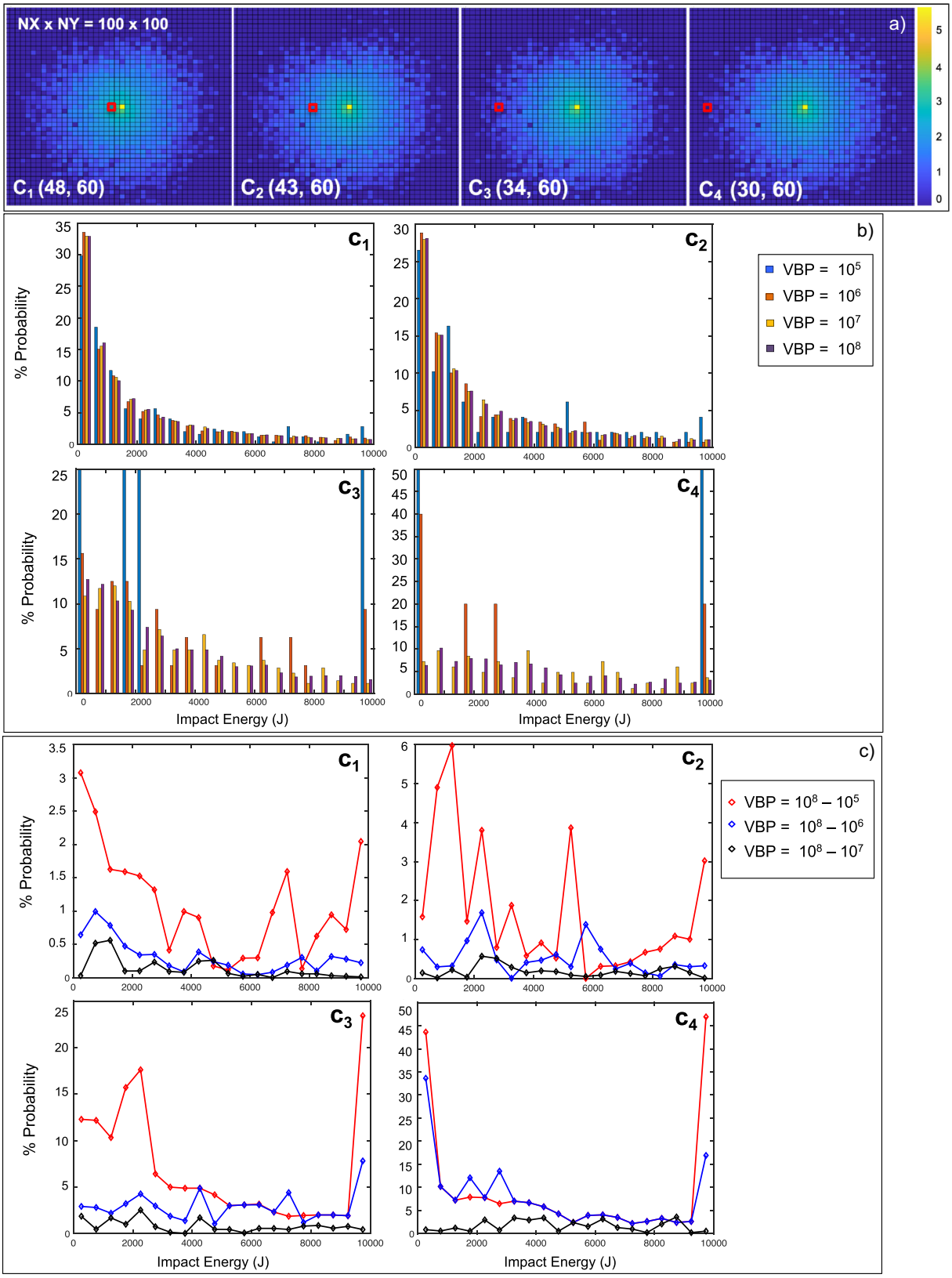

Fig. 5. a) Map showing the Log_{10} of the number of VBPs fallen in each cell of the domain, in the case of 10^7 clasts ejected. ESPs are from Table 3. In red the location of the four cells (c_1, c_2, c_3, c_4) selected for the sensitivity analysis. b) Probability (%) of ballistic impact energy for 20 energy classes for different numbers of VBPs launched in simulations: cell c_1, dome area, ca. 500 m from vent; cell c_2, Hospital, ca. 2600 m from vent; cell c_3, centre of *St.* Claude, ca. 4000 m from vent; d) cell c_4, point at ca. 5200 m from the vent. The cell coordinates referred to the grid with resolution of 100 × 100 are reported in bracket; c) Probability (%) curves showing the absolute difference between the probability associated to different numbers of released VBPs ($|10^8–10^5|$ red line, $|10^8–10^6|$ blue line, and $|10^8–10^7|$ black line), for cells c_1, c_2, c_3, c_4. The cell coordinates referred to the grid with resolution of 100 × 100 are reported in brackets.

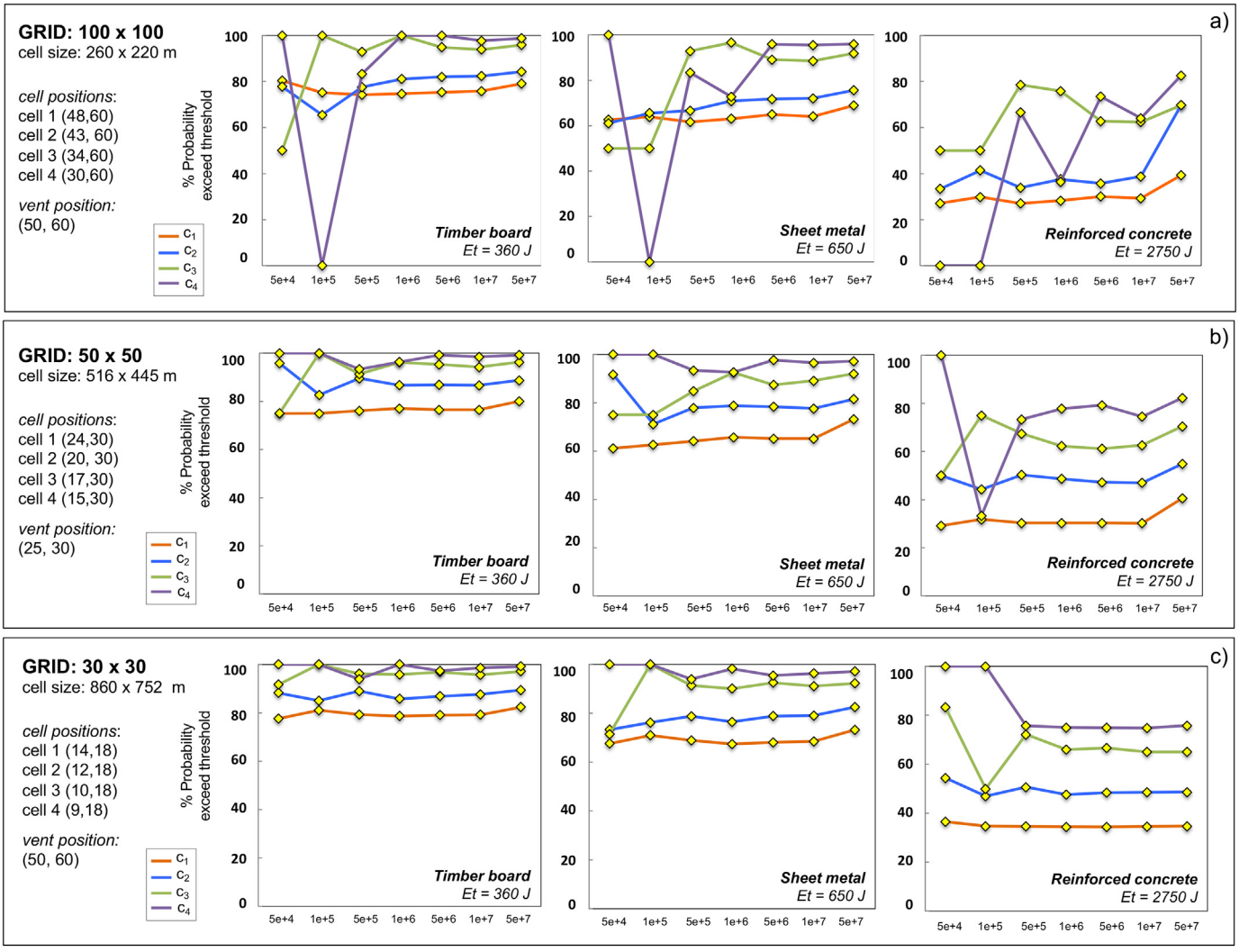

Fig. 6. Sensitivity of the probabilistic hazard assessment strategy for the number of released VBPs with respect to the resolution of the grid used to quantify the probability (%) of VBPs exceeding a given energy threshold E_t: a) 100 × 100 cells; b) 50 × 50 cells; c) 30 × 30 cells. The four lines represent the four cells on which probabilities were calculated (cell c_1, orange, cell c_2, blue, cell c_3, green, cell c_4, violet) at different grid resolutions. The cell coordinates referred to a)-b)-c) resolution grids are reported in brackets.

4.3. Sensitivity analysis on wind

In order to assess the effect of the wind on simulation results, we take into account the minimum and maximum wind speeds with their associated direction (minimum values: $W_s = 2$ m s^{-1}, $W_d = 279°$; maximum values: $W_s = 25$ m s^{-1}, $W_d = 343°$) measured during 2017–2018 from the local meteorological station "Piton Sanner" located at the summit dome (ca. 1467 m; Fig. 1d). We fixed a 860 m × 752 m (30 × 30 cells) grid resolution, and 2×10^6 simulated VBPs ejected from a single vent in the central part of the dome (643,664 E, 1774624 N, UTM coordinate system). In Fig. 7a we show the relative difference in the conditional exceedance probability $\theta^{ec}_{(A_{ij},E_t)}$ to overcome the selected energy thresholds (Table 3) obtained by comparing results with minimum wind conditions and in absence of wind. The differences are less than 5% for E_{t1} and E_{t2} (panels i-ii), and reach values up to 15% for E_{t3} (panel iii) in few cells, showing unstable relative differences (incoherent pattern for adjacent cells) at greater distances. Very similar results are obtained considering the maximum and absent wind conditions Fig. 7b).

Considering this, we conclude that wind does not significantly affect the probability results within a few km from the vent. This is in agreement with Biass et al. (2016) who simulated a mean wind with a constant velocity and direction, justified by the typically low altitudes reached by VBPs (<2 km on Vulcano island, Italy). Their results show that the final probabilities are not significantly affected by wind conditions since the smallest VBPs are the most influenced by wind, and fall near the vent due to the *caprock assumption* which is referred to the ejection of magma as a coherent plug (caprock) accelerated by the gas expansion up to a maximum velocity that breaks the plug in individual ballistic blocks (e.g., Self et al., 1979; Fagents and Wilson, 1993). As a result, the proximal probabilities are dominated by VBPs which are not strongly affected by wind advection. Moreover, the very few large VBPs can reach more distal areas but the wind has no influence on them, therefore their additional displacement is not able to alter the final probability values in distal cells.

4.4. Sensitivity analysis on the vent position

In this Section, we provide the sensitivity analysis to the position of the vent on the computational domain. In Fig. 8 we show the comparison between the conditional exceedance probabilities $\theta^{ec}_{(A_{ij},E_t)}$ for E_{t_3} (2750 J; Table 3) derived from *i)* assuming one hypothetical scenario

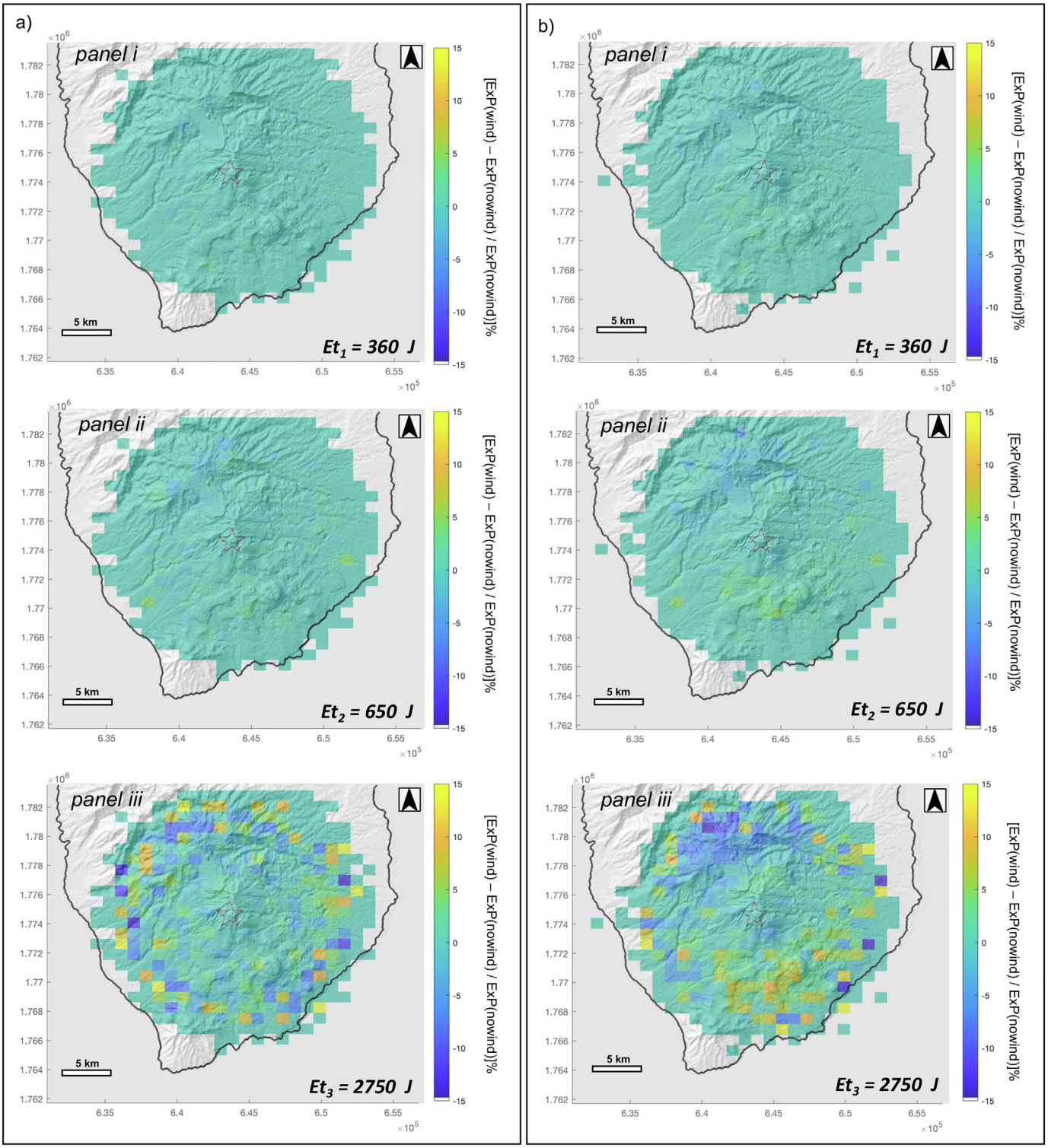

Fig. 7. Sensitivity analysis on wind conditions showing the relative difference between the exceedance probabilities $\theta^{ec}{}_{A_{ij},m}$ referred to $E_{t1} = 360$ J (panel i), $E_{t2} = 650$ J (panel ii), and $E_{t3} = 2750$ J (panel iii), in case of a) minimum ($W_s = 2$ m s^{-1}, $W_d = 279°$) and absent wind conditions. The same test was carried out in considering b) maximum ($W_s = 25$ ms^{-1}; $W_d = 343°$) and absent wind conditions. For all tests, the vent is located at the centre of the dome area (star).

of a single vent (for which we assume to be certain about position on the dome; Figs. 8a-b) and *ii)* considering the uncertainty on vent position, combining more vents (Fig. 8c). All results are provided in absence of wind.

Figs. 8a and b show the probability maps obtained by using two different single vents located on the dome (without considering the spatial uncertainty). Despite the two vents being positioned a few meters apart, a very different VBP dispersion pattern is observed, likely due to the effect of the local topography. For example, considering the south-west sector of the volcano (where the two most densely populated towns close to La Soufrière: St. Claude and Basse-Terre), the observed probabilities differ significantly in the two cases. In one case, indeed,

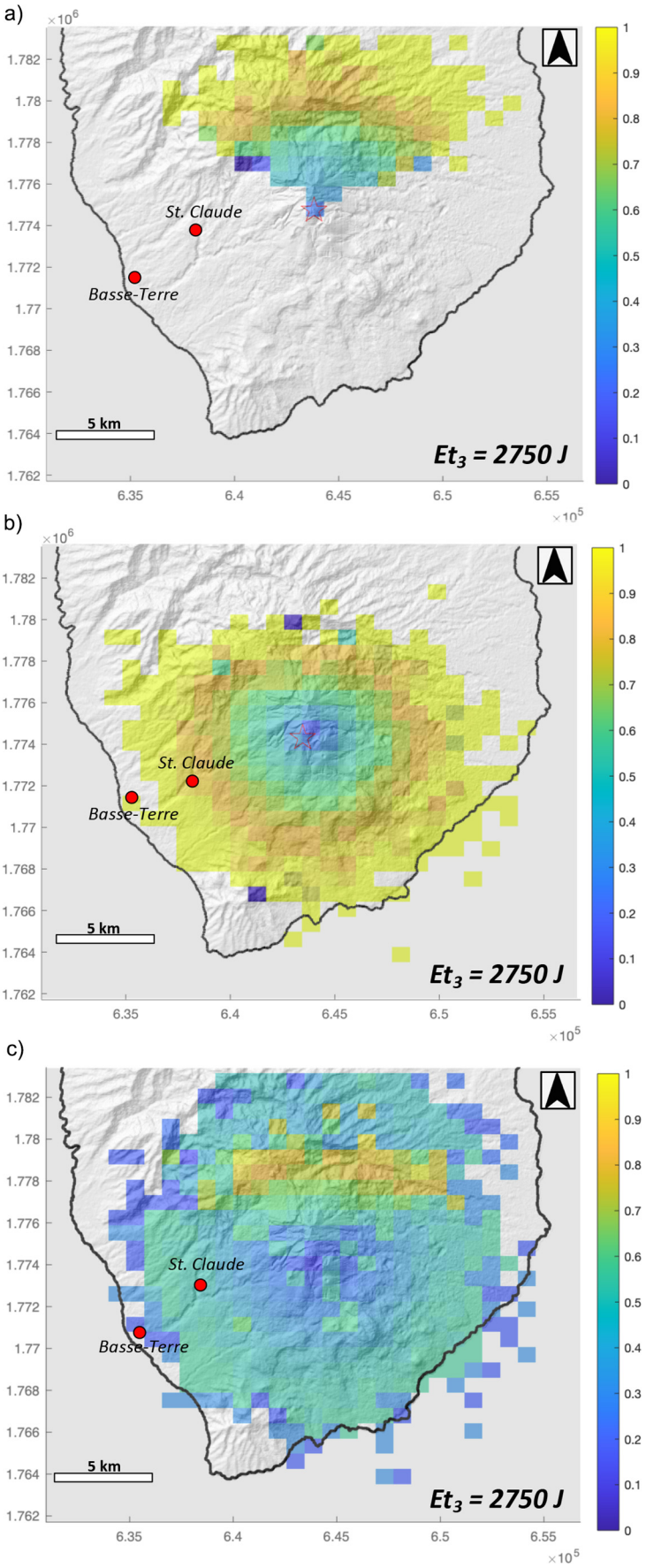

Fig. 8. Probability maps $\theta^{ec}{}_{A_{ij},m}$ to exceed E_{t3} (2750 J) considering the hypothetical scenario of a single vent located at a) 643820 E; 1,774,748 N (altitude: 1416 m), and b) 643,451 E; 1,774,316 N (altitude: 1273 m); c) Probability map $\theta^{e}{}_{A_{ij},m}$ to exceed E_{t3} (2750 J) considering the uncertainty on vent opening through the combination of more vents on the dome area.

we observe the released VBPs are strongly directed to the northern sector (Fig. 8a), leading to E_{t_3}negligible probability in the south west sector. On the contrary, in the case of Fig. 8b, the VBPs are radially more dispersed, leading to a non negligible probability in this sector.

Fig. 8c shows the conditional probability $\theta^{ec}{}_{A_{ij},m}$ to overcome E_{t3} taking into account the uncertainty of vent opening (according to eq. 9). Here, the exceedance probabilities of ca. 50–60% affected the major part of the Bass-Terre island, also showing lower values (ca. 20–30%) within ca. 5 km from the dome area. Only a limited area in the northern sector of the domain is affected by higher probability (ca. 80–90%). It is worth noting that the uncertainty on the vent position (Fig. 8c) "blurs" the resulting hazard or probability maps (e.g., Sandri et al., 2016); however, it represents more "honestly" our degree of knowledge on future eruptions (for which we actually do not know the effective vent position), leading to spatially unbiased probability maps.

5. Results

5.1. Spatial probability of vent opening

The sensitivity analysis to the position of the vent (Section 4.4) highlights how the spatial variability of vents opening is pivotal in this hazard assessment study since the resulting impact could affect the surrounding community at multiple scales in case of the adopted scenario.

The best-guess probability map for future vent opening at La Soufrière that we achieve is shown in Fig. 2a. This map shows that, while vents may be expected over very large areas, the probability that vent opens within the dome area is ca. 70%. For this reason, to limit the computational effort, we preliminary focus on this area.

In Fig. 2c, we report a zoom on the dome area showing the local variation of the spatial probability due to the most frequent historical and present-day vent openings close or along to the reactivated fractures and faults. In particular, in the northern sector of the dome are located numerous fractures (e.g., the 1960 fracture du Nord-Est, the 1797–98 fracture du Nord-Ouest and Faujas, the 1809–12 Fente du Nord fracture along Ty fault, reactivated during 1976–77; Fig. 1c), past thermal springs (e.g., 1836–37), craters (e.g., cratère Dupuy) and new high-flux fumaroles appeared since April 2018 and March 2019 (Fig. 1c). The central and the southwestern sectors host about twenty recent fumaroles (active from 2007 to 2018), few acid boiling pounds and six sites of hydrothermal fluid resurgence occurred during hydrothermal-phreatic eruptions (1797–98, 1836–37,1956,1976), mainly displaced along the Cratère Sud, 1956, 8/07/1976, Lacroix fractures (Fig. 1c). Along the flanks of the dome traces of other fumaroles and thermal springs are also observed (active since 1976–77 and 2017–2018; Fig. 1c).

The selected four macroareas (*A1, A2, A3, A4;* Fig. 2c) mark off these features, having in their centres the vent locations used for the GBF simulations that we carry out to provide the following hazard maps.

5.2. VBP hazard results

In this section, we provide the hazard results from the GBF simulations. The computational domain resolution is set to 30 × 30 cells (i.e. 860 m × 752 m) while the number of simulated clasts is set to 2×10^6 (Section 4).

Fig. 9a shows the overall exceedance probability $\theta^{e}{}_{A_{ij},m}$ for the selected energy thresholds, in absence of wind, conditional on the ejection of a clast during an eruption within the adopted scenario and from the dome, according to eq. (10). In red contours on a Log_{10} scale, the component $\theta^{f}{}_{A_{ij}}$ which is the probability that a VBP reaches the cell A_{ij} (weighted by ω'_k). This factor is not known a priori for each eruptions, therefore it does not make possible the calculation of probability conditional on the eruption (with a high number of VBPs).

Fig. 9b shows the exceedance probability $\theta^{ec}{}_{A_{ij},m}$ for the three energy thresholds E_{t1}, E_{t2}, E_{t3} (Table 3) in absence of wind, conditional on the ejection of a clast during an eruption within the adopted scenario and from the dome, according to eq. (9).

$\theta^{e}{}_{A_{ij},m}$ describes the product between the probability that a clast reaches the cell A_{ij} and that its impact energy exceeds the given threshold E_t, weighted by ω'_k (eq. 7). These two components have opposite trends in space. In Fig. 9a, we observe that $\theta^{e}{}_{A_{ij},m}$ varies from ca. 2% up to 40% for E_{t1}(360 J) and E_{t2} (650 J), exclusively within a few km around the dome but negligible elsewhere. For E_{t3} (2750 J) it varies up to 20%.

These values appear much lower than the conditional probability $\theta^{ec}{}_{A_{ij},m}$ shown in Fig. 9b, indicationg that a large portion of Basse-Terre island would be affected by hazard potentially leading to roof perforation with a probability in the range of 40–60% for $E_{t1}$and E_{t2}(panels i-ii). Smaller probabilities (from ca. 20 to 40%) are shown for E_{t3} (panel iii). As seen in Section 4.4, the uncertainty on vent position causes higher exceedance probability on the northern sector of the domain with respect to the choice of a single vent (Figs. 8a-b). However, these high probabilities are balanced by the fact that only very few and very-high energy VBPs are able to land very far from the vent.

5.3. Exposed elements and analysis of the potential impact

The built environment in Basse-Terre island has been described in Spence et al. (2008) where an integrated multi-risk impact analysis for the 1530 CE sub-Plinian eruption scenario is discussed (Boudon et al., 2008; Komorowski et al., 2008). Twenty building classes were identified (from BDTOPO digital database, National Institute of Geography IGN; Spence et al., 2008) for different impact zones in order to describe the differences between buildings, age and stories. Data by Spence et al. (2005) and Pomonis (2006) show that the buildings surrounding the volcano (not inclusive of all the area that could be potentially impacted) are made by reinforced concrete type for 57%, by masonry MW (medium weak) type for 30% and by timber MW to WE (weak) type for 13%. In particular, the most frequent types in St. Claude and Basse-Terre include masonry, timber and reinforced concrete materials (see Fig. 2 in Spence et al., 2008).

The last updated information we found about inhabitants is referred to 2018 indicating 88,300 people living within a radius of 15 km from the volcano (Leone et al., 2018).

In this section, we use a first-order approach to combine the exposed elements (i.e., schools, hospitals and clinics, towns, villages, and the airport) with the probability maps in absence of wind (Fig. 9). The probability maps shown in Fig. 10 provide an opportunity to identify the main urban areas likely to be impacted in case of an eruption of the adopted scenario from the dome area.

Only considering the impact energy, in Fig. 10 (panels a-b-c) we overlap the exposure map with the probability $\theta^{ec}{}_{A_{ij},m}$ to overcome the investigated energy thresholds in the most important urban centres of the Bass-Terre island. In particular, St. Claude shows higher probabilities (ca. 50–60%) which in some few areas appeared ≥60% (as two residential agglomerates belonging to *St.* Claude Municipality located in the proximity of volcanic edifice, Matouba at ca. 3.4 km and Papaye at ca. 2.9 km from the dome; Komorowski et al., 2008). Towards the coastline, Basse-Terre is characterised by the probability to exceed the energy thresholds of 30–40%, not covering the whole town.

In Fig. 10 (panels d-e-f), the frequency of the fallen clasts in the cell A_{ij} is also taken into account therefore we overlap the exposure map with the overall probability $\theta^{e}{}_{A_{ij},m}$ to overcome the investigated energy thresholds, showing that only a limited area (<3 km from the dome) is affected by the probability to overcome the energy thresholds, from ca. 2 up to 40%. In this case, only sparse inhabited areas would be exposed to the VBP hazard. The same observation can be made for the

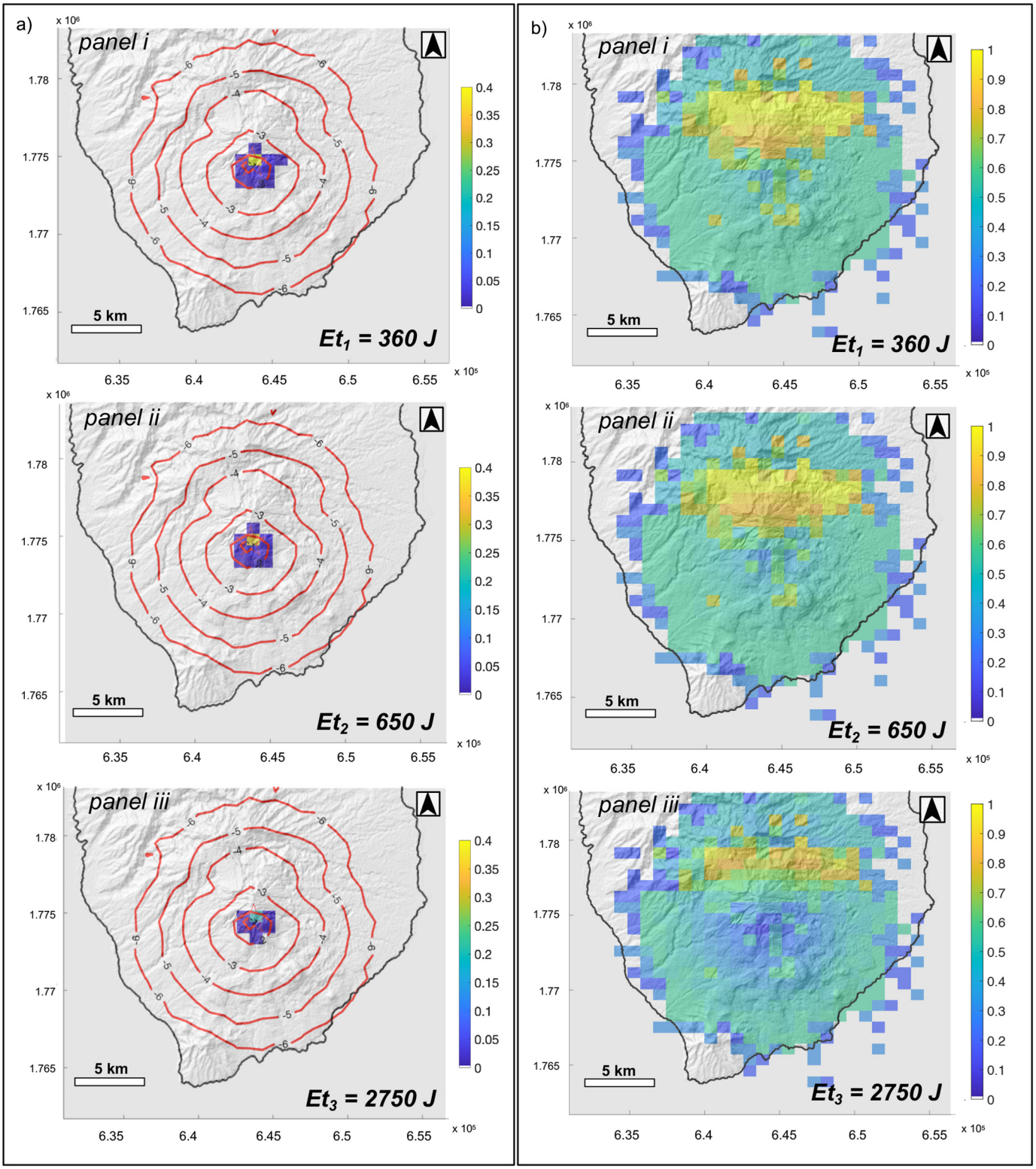

Fig. 9. a) Probability maps $\theta^{e}{}_{A_{ij},m}$ of VBPs exceeding energy thresholds (Table 3; panels i-ii-iii) in absence of wind, according to the eq. (10). Red contours represent the Log_{10} of the component $\theta^{f}{}_{A_{ij}}$ which is the probability that a VBP reaches the cell A_{ij} weighted for ω'_k. All probabilities are conditional to the ejection of a clast during an eruption within the adopted scenario and from the dome; b) Probability maps $\theta^{ec}{}_{A_{ij},m}$ of VBPs exceeding energies thresholds (Table 3; panels i-ii-iii) in absence of wind, according to eq. (9).

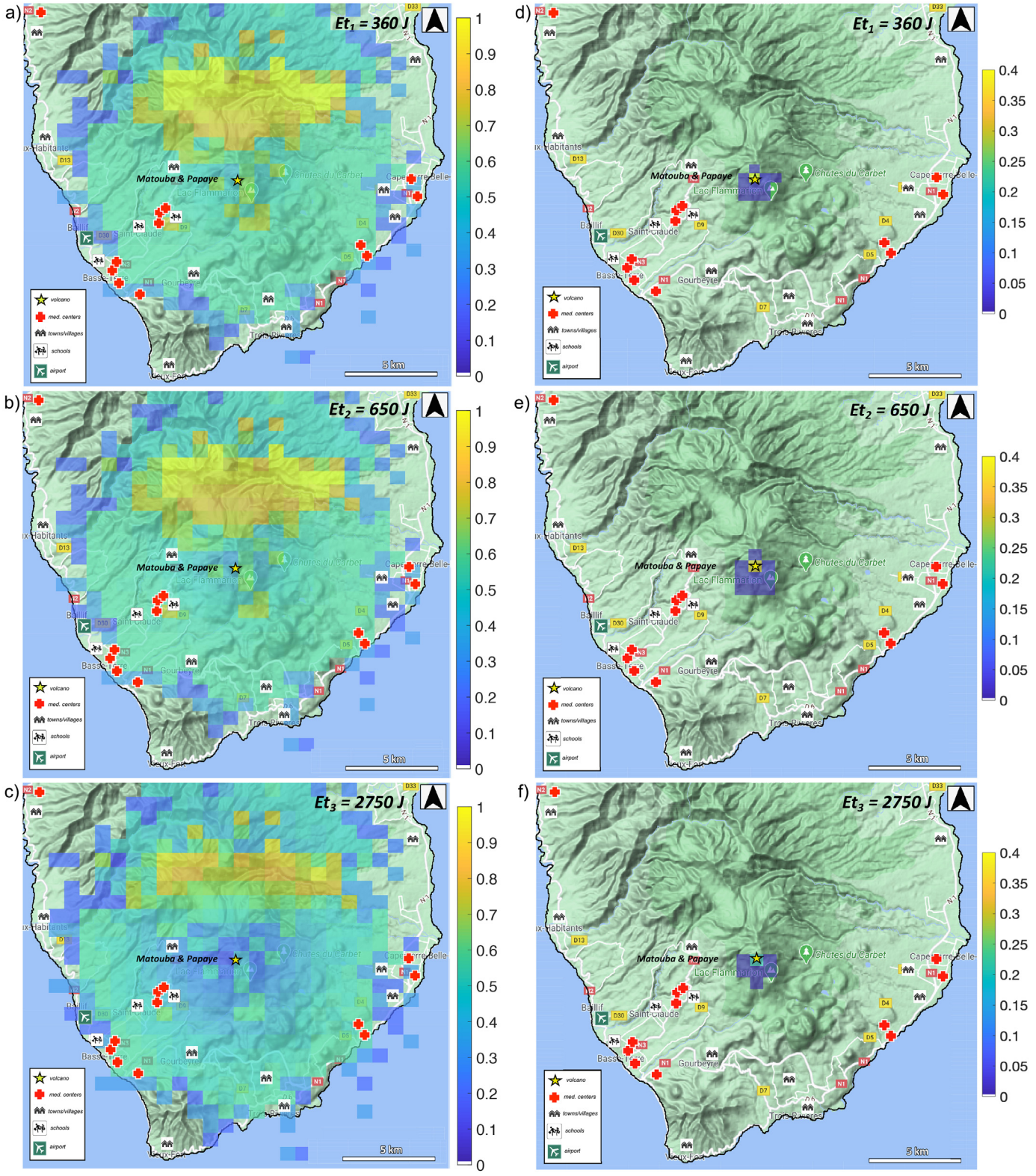

Fig. 10. Exposure-based risk analysis considering the conditional probability $\theta^{ec}{}_{A_{ij},m}$ (a-b-c) and the overall probability $\theta^{e}{}_{A_{ij},m}$ (d-e-f) of VBPs exceeding selected energy thresholds (Table 3). All probabilities are conditional to the ejection of a clast during an eruption within the adopted scenario and from the dome, in absence of wind. Symbols in legend: yellow star: La Soufrière volcano; red cross: hospitals and clinics; two-houses: towns (i.e., *St.* Claude, Basse-Terre) and villages (i.e., Matouba and Papaye); running children: schools; airplane: airport). The location of each element has been identified at https://www.google.it/maps.

other towns along the coastline (i.e. Baillif, Vieux-Habitants and Capesterre) and the urban connections along both sides of the coast, with the exception of Vieux-Fort and a large part of Trois-Rivieres which result not affected by VBPs.

However, as described in Fitzgerald et al. (2014), the infrastructures at risk of ballistic impact not only include buildings (including hospitals, clinics, commercial and residential properties, schools) but also footpaths, unpaved tracks and paved roads. These latter around La Soufrière are very busy with tourists, guides and OVSG-IPGP operators during a large part of the year. Further work is required to characterise accurately the number of visitor (estimated in 2011 at 76000–134000 per year; https://guadeloupe-parcnational.com/IMG/pdf/communique-de-presse.pdf) and to quantify the exposure of people to the VBP's impact.

6. Discussion

6.1. Vent opening and VBP hazard for Guadeloupe

Defining likely locations of future vents is a challenging goal of volcanology and a pivotal element for volcanic hazard assessment. Therefore, a vent opening map is key to provide adequate hazard maps, in particular for volcanic fields and calderas where the uncertainty on location of a future vent is much larger (e.g., Connor et al., 2000; Orsi and Isaia, 2004; Rougier and Beven, 2013).

In the last decades, many probabilistic maps have been provided for calderas through quantitative analysis based on geophysical, geological and geochemical parameters or by Bayesian inference procedures (Campi Flegrei; e.g., Alberico et al., 2002; Selva et al., 2012; Okataina Volcanic Centre, New Zealand; Thompson et al., 2015). Further probabilistic analyses have been also used, including the main sources of epistemic uncertainty about the volcanic system through a structured expert elicitation (e.g., Campi Flegrei; Bevilacqua et al., 2015; Somma-Vesuvius; Tadini et al., 2017).

No similar study has been conducted in Guadeloupe, overlooking the identification of likely future vent locations even though La Soufrière was formed within the edifice-collapse depression of the Grande Découverte–Soufrière volcanic complex (e.g., Komorowski, 2005).

Here, for the first time, we compile a spatial probability map of vent opening by incorporating the up-to-date information on the distributions of past vents, faults and fractures as well as the past and present-day observed fumaroles (Fig. 1c). In this framework, this kind of maps represent a crucial input information for a future development of quantitative (VBP) hazard and risk maps of eruptive phenomena at La Soufrière.

Moreover, our hazard results can be compared with probabilistic maps based on the 1888–90 CE Vulcanian eruption at Vulcano island (Italy) proposed by Biass et al. (2016), where urban areas are located within a radius of 1 km around the most active vent (La Fossa). In that case, the impact energies are in the range of $0.06–4 \times 10^6$ J at distances between 1 and 1.5 km from the vent. Hazard and vulnerability aspects together produce a pre-event impact assessment showing the potential number of affected buildings by extrapolating the tephra fallout vulnerability curves for European roofs (Spence et al., 2005) to the impact of VBPs. Slight differences in the final probability values are shown for the energy thresholds of 60 J (related to the perforation of weak tile roofs) and 8000 J (related to the perforation of strong armoured roofs). The urban agglomerates of Porto (1.3 km N of the vent) and Lentia (1.8 km NW of the vent) are the most exposed areas having probabilities to overcome the selected thresholds of ca. 10^{-2}% and ca. 5×10^{-3}%, respectively. Other more distant settlements (as Il Piano and Vulcanello) located at ca. 2.4 km SW and 2.6 km N of the vent show lesser probabilities of 7×10^{-4}% and 4×10^{-4}%, respectively.

For La Soufrière, the exposure-based risk maps shown in Fig. 10a reveal that the overall probability to overcome the energy thresholds (Table 3) is in the order of 10^{-2}% within 1–2 km from the dome area, similar to the exceedance probabilities around Porto and Lentia, at Vulcano island. Finally, as demonstrated in Section 4.3, in the GBF model the influence of wind on ballistic trajectories is negligible since only a few large VBP impact more distal areas.

6.2. Comparison with other eruption scenarios at La Soufrière

The most relevant eruptive scenario for clasts is the 1530C.E.-like sub-Plinian scenario (as reported in the analysis by Hincks et al. (2014), which was already investigated by Komorowski (2005); Komorowski et al. (2008) and Esposti-Ongaro et al. (2020). Komorowski et al. (2008) provided an assessment of the overall risk levels that can be reached for different areas of Saint-Claude and Basse-Terre, showing a very high risk level over short distances from the vent. For instance, around Matouba (*St*. Claude Municipality, 3.4 km from the vent) there is a 81% probability that the isomass threshold (138 kg m^{-2}) will be exceeded considering a set of daily winds randomly sampled in 5 years. On the contrary, in Saint-Claude (4.15 km from the vent) the same exceedance probability is sharply reduceed to 38%, corresponding to a static pressure load of 2 kPa, that is a critical value to start the damage on the weakest roofs.

Recently, Esposti-Ongaro et al. (2020) assessed the factors controlling PDCs (i.e., propagation and hazards) in case of a subplinian eruption scenario at La Soufrière by using a deterministic approach, revealing that subplinian eruptions can display a wide range of eruptive styles with different impacts from associated PDCs although within a short range of mass eruption rates. This outcome represents an important contribution to the quantitative assessment of volcanic hazard and risk at La Soufrière, taking into account the present-day unrest of the volcano.

Komorowski (2005) presented a multi-hazard map based on five likely eruptive scenarios. Three of these are the most likely: i) *scenario 2* including phreatic eruptions which would be the most likely as the most frequent in the last 15 kyr, ii) *scenario 3* about the edifice collapse eruptions which could involve both the SW and SE flanks of the volcano affecting the populations of Saint-Claude, Basse-Terre, Gourbeyre and Trois-Rivières for a total estimated population of ca. 39.000 and up to ca.58.600, and iv) *scenario 4* regarding the dome eruptions such as the 1530C.E. eruption, would also affect the major southern part of Basse-Terre island. The multi-hazard map includes four hazard zones for the southern Basse-Terre island (see Figure on pag. 96 in Komorowski, 2005), showing the areas most likely impacted by the five eruptive scenarios for vent opening on or within 1 km the dome, and the presence of easterly trade winds between 0 and ca. 7 km altitude. In particular, *"Zone 2B"* (see Figure on pag. 96 in Komorowski, 2005) includes the hazard zones for debris avalanches occurred in the last 15.000 years and those likely to be covered by VBPs.

In this framework, our probabilistic hazard assessment is based on the occurrence of phreatic, Vulcanian and Strombolian eruptions, and it could be used to quantify the VBPs impacts with a good level of confidence within "*Zone 2B*", which is where the highest level of hazards are superimposed (see Figure on pag. 96 in Komorowski, 2005). The initial conditions are referred to an averaged scenario of explosive styles (including phreatic, Vulcanian and Strombolian eruptions) in order to explore a large set of input parameters. Although the most recurrent eruptions at La Soufrière were phreatic, Vulcanian and Strombolian eruptions also occurred between 6535 BCE to 1635 characterised by VEI 2–4, with dome growth, blast and edifice collapses (Boudon et al., 1988, 2007, 2008; Komorowski, 2005; Komorowski et al., 2008; Siebert and Simkin, 2002–2011). According to Komorowski (2005), our first-order exposure analysis (Fig. 9) shows that the buildings affected by roof perforations are within ca. 3 km the La Soufrière dome. This implies that the urban agglomerates as Papaye, Matouba and the northeastern part of *St*. Claude would be affected. On the contrary, the "*Zone 3*" and "*Zone 4*" (see Figure on page 96 in Komorowski, 2005) correspond to areas where the exceedance probabilities are not reliable,

and given their moderate and low hazards, it is unlikely that they can be affected by VBP impacts.

7. Conclusions

Our results represent the very first study to quantify the hazard posed by VBP impacts associated with the occurrence of phreatic, Vulcanian and Strombolian eruptions at La Soufrière, considering the spatial uncertainty on vent opening. Moreover, the proposed hazard assessment could be an important factor to be considered in the framework of the "blue-sky" eruptions (i.e., unexpected or not preceded by any recognized increase in activity; Doherty, 2009) since their recognition implies a significant risk to people living near, or on the volcano at the eruption time.

Following the model of Biass et al. (2016), we provide a new MATLAB routine for the GBF post-processing (see Supplementary Material) based on a new approach for calculating the occurrence probability of VBP impacts that exceed selected energy thresholds (Table 3) hazardous for the built environment of Guadeloupe (i.e., Spence et al., 2005, 2008; Williams et al., 2017). In the following, a brief summary of the main outcomes of this work is reported:

1) A spatial map of vent opening, conditional on the occurrence of a volcanic eruption from the adopted eruptive scenario, has been provided following the approach in Selva et al. (2012). The estimates are based on the geological information, historical eruptive vents and observed fumarolic activity;
2) Sensitivity analyses have been carried out to explore the best number of simulated VPBs, the effects of wind and the position of the vent on model results. The tests show that:

- 2×10^6 is the optimum number of VBPs that may be released on 30×30 cells (i.e. 860 m $\times$ 752 m) resolution grid balancing the result stability and computational costs;

- the final hazard maps are not significantly affected by the wind advection within a radius of 5 km from the vent. This is also in agreement with Biass et al. (2016);

- remarkable differences are observed *a*) when simulations account for a single vent as hypothetical scenario and *b*) for the uncertainty on vent opening from the dome area;

3) A new approach has been proposed to calculate the probability to exceed the energy thresholds E_{t_m} ($m = 1,2,3$) that are relevant for roof perforations, conditional to the ejection of a clast during an eruption within the adopted scenario and from the dome. We separate the conditional probabilities in two components:

- the conditional probability $\theta^{ec}{}_{A_{ij},m}$ to exceed a given threshold E_t when a VBP falls in the cell A_{ij};
- the overall probability $\theta^{e}{}_{A_{ij},m}$ that a clast reaches the cell A_{ij} and that its impact energy exceeds the given threshold E_t.

The conditional probability and its components are computed by accounting for uncertainty in vent location, that is, the probabilities from each single vent are "weighted" for the vent opening probability ω'_k (which is normalized to the dome area).

4) Hazard and exposure aspects have been combined to produce an exposure-based qualitative risk map. Considering $\theta^{ec}{}_{A_{ij},m}$, the results show that a large portion of the Basse-Terre town would be affected by the VBP impacts that exceed the energy thresholds for roof perforation with a probability in the range of 20–60%, with the exception of a limited sector showing a higher probability (>80%). On the contrary, when the overall probability $\theta^{e}{}_{A_{ij},m}$ is accounted for, the probability is exclusively restricted to a few kilometres from the dome area and shows lower values to overcome the selected energy thresholds (from ca. 2% up to 40%). This means that in areas where urban agglomerates are within a few km from the vent such is the case at La Soufrière, the choice of a probabilistic approach is key to estimate the likelihood of occurrence of VBPs impacts as a first step towards the development and implementation of pro–active risk reduction strategies.

Credit author statement

S.M., E.R, L.S., C.B and J.S. have conceived the methodology adopted in this project. S.M. and E.R. have adapted the software for the application to La Soufrière de Guadeloupe volcano and carried out the simulations. R.M. and J.C.K. have helped to constrain the hazard scenario considered and provided the data required for model validation. S.M. has written the first draft of the manuscript. All authors have contributed to the writing and finalization of the paper.

Scripts for the vent opening probability and post-processing

The Python script for spatial probabilities on vent opening and the MATLAB post-processing routine for calculating $\theta^{ec}ec$and θ^{e} are open-source on a GitHub repository at: https://github.com/silfromitaly1/probabilistic_hazard_assessment_for_ballistics

Declaration of Competing Interest

None.

Acknowledgements

SM, CB, LS, JS, RM and JCK were supported by the European Union's Horizon 2020 project EUROVOLC (grant agreement no. 731070). We thank K. Nemeth and an anonymous reviewer for their constructive comments and the Editor for the handling of the manuscript.

Appendix A. Supplementary data

Supplementary data to this article can be found online at https://doi.org/10.1016/j.jvolgeores.2021.107453.

References

Alatorre-Ibargüengoitia, M., Delgado-Granados, H., Dingwell, D., 2012. Hazard map for volcanic ballistic impacts at Popocatépetl volcano (Mexico). Bull. Volcanol. 74, 2155–2169.

Alberico, I., Lirer, L., Petrosino, P., Scandone, R., 2002. A methodology for the evaluation of long-term volcanic risk from pyroclastic flows in Campi Flegrei (Italy). J. Volcanol. Geotherm. Res. 116, 63–78.

Allard, P., Aiuppa, A., Beauducel, F., Gaudin, D., Di Napoli, R., Calabrese, S., Parello, P., Crispi, F., Hammouya, G., Tamburello, G., 2014. Steam and gas emission rate from La Soufriere volcano, Guadeloupe (Lesser Antilles): implications for the magmatic supply during degassing unrest. Chem. Geol. 384, 76–93.

Bevilacqua, A., Isaia, R., Neri, A., Vitale, S., Aspinall, W.P., Bisson, M., Flandoli, F., Baxter, P.J., Bertagnini, A., Esposti-Ongaro, T., Iannuzzi, E., Pistolesi, M., Rosi, M., 2015. Quantifying volcanic hazard at Campi Flegrei caldera (Italy) with uncertainty assessment:1.Vent opening maps. J. Geophys. Res. Solid Earth 120, 2309–2329. https://doi.org/10.1002/2014JB011775.

Biass, S., Scaini, C., Bonadonna, C., Folch, A., Smith, K., Höskuldsson, A., 2014. A multi-scale risk assessment for tephra fallout and airborne concentration from multiple Icelandic volcanoes - part 1: hazard assessment. Nat. Hazards Earth Syst. Sci. 14, 2265–2287.

Biass, S., Falcone, J.L., Bonadonna, C., Di Traglia, F., Pistolesi, M., Rosi, M., Lestuzzi, P., 2016. Great Balls of Fire: a probabilistic approach to quantify the hazard related to ballistics: a case study at La Fossa volcano, Vulcano Island. Italy. J. Volcanol. Geotherm. Res. 325, 1–14.

Blong, R.J., 1981. Some effects of tephra falls on buildings. Tephra studies. Springer, Dordrecht, pp. 405–420.

Blong, R.J., 1984. Volcanic Hazards. Academic Press, Orlando, A Sourcebook on the Effects of Eruptions.

Blong, R., 2000. Volcanic Hazards and Risk Management. In: Sigurdsson, H., Houghton, B., Stephen, McNutt, Rymer, H., Stix, J. (Eds.), Encyclopedia of Volcanoes. Academic Press, pp. 1215–1227.

Boichu, M., Villemant, B., Boudon, G., 2008. A model for episodic degassing of an andesitic magma intrusion. J. Geophys. Res. Solid Earth 113 (B7).

Boichu, M., Villemant, B., Boudon, G., 2011. Degassing at La Soufrière de Guadeloupe volcano (Lesser Antilles) since the last eruptive crisis in 1975–77: result of a shallow magma intrusion? J. Volcanol. Geotherm. Res. 203 (3–4), 102–112.

Bonadonna, C., Biass, S., Menoni, S., Gregg, C.E., 2021. Assessment of risk associated with tephra-related hazards. In: Papale, P. (Ed.), Forecasting and Planning for Volcanic Hazards, Risks, and Disasters. [s.l.]. Elsevier(Hazards and Disasters), pp. 329–378 https://doi.org/10.1016/B978-0-12-818082-2.00008-1.

Booth, B., 1979. Assessing volcanic risk. J. Geol. Soc. 136 (3), 331–340.

Boudon, G., Dagain, J., Semet, M., Westercamp, D., 1988. Carte et notice explicative de la carte géologique du massif volcanique de la Soufriere (Département de la Guadeloupe, Petites Antilles), scale 1: 20,000. Bur. de Rech. Geol. et Min, Orléans, France.

Boudon, G., Le Friant, A., Komorowski, J.C., Deplus, C., Semet, M.P., 2007. Volcano flank instability in the Lesser Antilles Arc: diversity of scale, processes, and temporal recurrence. J. Geophys. Res. 112, B08205.

Boudon, G., Komorowski, J.C., Villemant, B., Semet, M.P., 2008. A new scenario for the last magmatic eruption of La Soufrière of Guadeloupe (Lesser Antilles) in 1530 a.D. evidence from stratigraphy radiocarbon dating and magmatic evolution of erupted products. J. Volcanol. Geotherm. Res. 178, 474–490.

Breard, E.C.P., Lube, G., Cronin, S.J., Fitzgerald, R., Kennedy, B., Scheu, B., Montanaro, C., White, J.D.L., Tost, M., Procter, J.N., Moebis, A., 2014. Using the spatial distribution and lithology of ballistic blocks to interpret eruption sequence and dynamics: August 6 2012 Upper Te Maari eruption. New Zealand. J. Volcanol. Geotherm. Res 286, 373–386.

Brothelande, E., Finizola, A., Peltier, A., Delcher, E., Komorowski, J.C., Di Gangi, F., Legendre, Y., 2014. Fluid circulation pattern inside La Soufrière volcano (Guadeloupe) inferred from combined electrical resistivity tomography, self-potential, soil temperature and diffuse degassing measurements. J. Volcanol. Geotherm. Res. 288, 105–122.

Casadevall, T.J., 1994. The 1989–1990 eruption of Redoubt Volcano, Alaska: impacts on aircraft operations. J. Volcanol. Geotherm. Res. 62 (1–4), 301–316.

Chenet, M., Grancher, D., Redon, M., 2014. Main issues of an evacuation in case of volcanic crisis: social stakes in Guadeloupe (Lesser Antilles Arc). Nat. Hazards 73, 2127–2147.

Clarke, A.B., Neri, A., Voight, B., Macedonio, G., Druitt, T.H., 2002. Computational modelling of the transient dynamics of the August 1997 Vulcanian explosions at Soufriere Hills Volcano, Montserrat: influence of initial conduit conditions on near-vent pyroclastic dispersal. Mem. Geol. Soc. London 21, 319–348.

Connor, C.B., Stamatakos, J.A., Ferrill, D.A., Hill, B.E., Ofoegbu, G.I., Conway, F.M., Sagar, B., Trapp, J., 2000. Geologic factors controlling patterns of small-volume basaltic volcanism: application to a volcanic hazards assessment at Yucca Mountain. Nevada. J. Geophys. Res. 105 (B1), 417–432.

Connor, C.B., Bebbington, M., Marzocchi, W., 2015. Probabilistic volcanic hazard assessment. In: The Encyclopedia of Volcanoes, 897–910. Press, Academic.

Costa, A., Dell'Erba, F., Di Vito, M.A., Isaia, R., Macedonio, G., Orsi, G., Pfeiffer, T., 2009. Tephra fallout hazard assessment at the Campi Flegrei caldera (Italy). Bull. Volcanol. 71 (3), 259.

de Michieli Vitturi, M., Neri, A., Esposti Ongaro, T., Lo Savio, S., Boschi, E., 2010. Lagrangian modeling of large volcanic particles: application to Vulcanian explosions. J. Geophys. Res. Solid Earth 115, B08206.

Del Negro, C., Cappello, A., Neri, M., Bilotta, G., Hérault, A., Ganci, G., 2013. Lava flow hazards at Mount Etna: constraints imposed by eruptive history and numerical simulations. Sci. Rep. 3 (1), 1–8.

Dellino, P., De Astis, G., La Volpe, L., Mele, D., Sulpizio, R., 2011. Quantitative hazard assessment of phreatomagmatic eruptions at Vulcano (Aeolian Islands, Southern Italy) as obtained by combining stratigraphy, event statistics and physical modelling. J. Volcanol. Geotherm. Res. 201 (1–4), 364–384.

Di Traglia, F., Pistolesi, M., Rosi, M., Bonadonna, C., Fusillo, R., Roverato, M., 2013. Growth and erosion: the volcanic geology and morphological evolution of La Fossa (island of Vulcano, Southern Italy) in the last 1000 years. Geomorphology 19, 94–107.

Dispositions Spècifiques ORSEC de La Guadeloupe: phènomènes volcaniques. https://www.guadeloupe.gouv.fr/content/download/15808/103240/file/Dispositions%20sp%C3%A9cifiques%20ORSEC%20de%20la%20Guadeloupe%20_%20Ph%C3%A9nom%C3%A8nes%20volcaniques.pdf.

Doherty, A.L., 2009. Blue-Sky Eruptions, Do they Exist?: Implications for Monitoring New Zealand's Volcanoes. PhD ThesisUniversity of Canterbury.

Druitt, T.H., Young, S.R., Baptie, B., Bonadonna, C., Calder, E.S., Clarke, A.B., Cole, P.D., Harford, C.L., Herd, R.A., Luckett, R., Ryan, G., Voight, B., 2002. Episodes of cyclic vulcanian explosive activity with fountain collapse at Soufrière Hills Volcano, Montserrat. In: Druitt, T., Kokelaar, B. (Eds.), The Eruption of Soufrière Hills Volcano, Montserrat, from 1995 to 1999 vol. 21. Geol. Soc. London, pp. 281–306.

Esposti-Ongaro, T., Komorowski, J.C., Legendre, Y., Neri, A., 2020. Modelling pyroclastic density currents from a subplinian eruption at La Soufrière de Guadeloupe (West Indies, France). Bull. Volcanol. 82-76. https://doi.org/10.1007/s00445-020-01411-6.

Fagents, S.A., Wilson, L., 1993. Explosive volcanic eruptions—VII. The ranges of pyroclasts ejected in transient volcanic explosions. Geoph. J. Int. 113 (2), 359–370.

Feuillard, M., Allegre, C.J., Brandeis, G., Gaulon, R., Le Mouel, J.L., Mercier, J.C., Semet, M.P., 1983. The 1975–1977 crisis of la Soufriere de Guadeloupe (FWI): a still-born magmatic eruption. J. Volcanol. Geotherm. Res. 16 (3–4), 317–334.

Fitzgerald, R.H., Tsunematsu, K., Kennedy, B.M., Breard, E.C.P., Lube, G., Wilson, T.M., Jolly, A.D., Pawson, J., Rosenberg, M.D., Cronin, S.J., 2014. The application of a calibrated 3D ballistic trajectory model to ballistic hazard assessments at upper Te Maari. Tongariro. J. Volcanol. Geotherm. Res. 286, 248–262.

Fitzgerald, R.H., Kennedy, B.M., Wilson, T.M., Leonard, G.S., Tsunematsu, K., Keys, H., 2017. The Communication and Risk Management of Volcanic Ballistic Hazards. In: Fearnley, C.J., Bird, D.K., Haynes, K., McGuire, W.J., Jolly, G. (Eds.), Observing the Volcano World. Advances in Volcanology an Official Book Series of the IAVCEI, Barcelona, Spain. Springer, Cham https://doi.org/10.1007/11157_2016_35.

Folch, A., Sulpizio, R., 2010. Evaluating long-range volcanic ash hazard using supercomputing facilities: application to Somma-Vesuvius (Italy), and consequences for civil aviation over the Central Mediterranean Area. Bull. Volcanol. 72 (9), 1039–1059.

Formenti, Y., Druitt, T.H., Kelfoun, K., 2003. Characterisation of the 1997 Vulcanian explosions of Soufrière Hills Volcano, Montserrat, by video analysis. Bull. Volcanol. 65 (8), 587–605.

Gaudin, D., Beauducel, F., Allemand, P., Delacourt, C., Finizola, A., 2013. Heat flux measurement from thermal infrared imagery in low-flux fumarolic zones: example of the Ty fault (La Soufrière de Guadeloupe). J. Volcanol. Geotherm. Res. 267, 47–56.

Gaudin, D., Beauducel, F., Coutant, O., Delacourt, C., Richon, P., de Chabalier, J.B., Hammouya, G., 2016. Mass and heat flux balance of La Soufrière volcano (Guadeloupe) from aerial infrared thermal imaging. J. Volcanol. Geotherm. Res. 320, 107–116.

Hincks, T.K., Komorowski, J.C., Sparks, S.R., Aspinall, W.P., 2014. Retrospective analysis of uncertain eruption precursors at La Soufrière volcano, Guadeloupe, 1975–77: volcanic hazard assessment using a Bayesian Belief Network approach. J. Appl. Volcanol. 3 (1), 3.

Houghton, B.F., Swanson, D.A., Biass, S., Fagents, S.A., Orr, T.R., 2017. Partitioning of pyroclasts between ballistic transport and a convective plume: Kīlauea volcano, 19 March 2008. J. Geophys. Res. Solid Earth 122 (5), 3379–3391.

Jenkins, S., Magill, C., McAneney, J., Blong, R., 2012. Regional ash fall hazard I: a probabilistic assessment methodology. Bull. Volcanol. 74 (7), 1699–1712.

Jenkins, S.F., Wilson, T.M., Magill, C., Miller, V., Stewart, C., Blong, R., Marzocchi, W., Boulton, M., Bonadonna, C., Costa, A., 2015. Volcanic ash fall hazard and risk. Global Volcanic Hazards and Risk 173–222.

Kilgour, G., Manville, V., Della Pasqua, F., Graettinger, A., Hodgson, K.A., Jolly, G.E., 2010. The 25 September 2007 eruption of Mount Ruapehu, New Zealand: directed ballistics, surtseyan jets, and ice-slurry lahars. J. Volcanol. Geotherm. Res. 191 (1–2), 1–14.

Komorowski, J.C., 2005. Guadeloupe. Volcanic Atlas of the Lesser Antilles. pp. 65–102.

Komorowski, J.C., 2015. Maps from Institute de Physique du Globe de Paris, France (complied and modified from Jolivet, 1958; Barrabè and Jolivet, 1958; Boudon et al., 1988; Komorowski et al., 2005, Feuillard, 2011, Legendre, 2012).

Komorowski, J.C., Legendre, Y., Caron, B., Boudon, G., 2008. Reconstruction and analysis of sub-plinian tephra dispersal during the 1530 AD Soufrière (Guadeloupe) eruption: Implications for scenario definition and hazards assessment. J. Volcanol. Geotherm. Res. 178 (3), 491–515.

Le Guern, F., Bernard, A., Chevrier, R.M, 1980. Soufriere of Guadeloupe 1976-1977 eruption-mass and energy transfer and volcanic health hazards. Bull Volcanol 43, 578–592.

Le Gonidec, Y., Rosas-Carbajal, M., de Bremond d'Ars, J., Carlus, B., Ianigro, J.C., Kergosien, B., Gibert, D., 2019. Abrupt changes of hydrothermal activity in a lava dome detected by combined seismic and muon monitoring. Sci. Rep. 9 (1), 1–9.

Legendre, Y., 2012. Reconstruction fine de l'histoire éruptive et scénarii éruptifs à la Soufrière de Guadeloupe: vers un modèle intégré de fonctionnement du volcan (Doctoral dissertation, Paris 7).

Leone, F., Komorowski, J.C., Gherardi-Leone, M., Lalubie, G., Lesales, T., Gros-Désormeaux, J.R., Deymier, J., 2018. Accessibilité territoriale et gestion de crise volcanique aux Antilles françaises (Guadeloupe & Martinique): contribution à la planification des évacuations. Cybergeo: European. J. Geogr. https://doi.org/10.4000/cybergeo.29425.

Loughlin, S.C., Sparks, R.S.J., Sparks, S., Brown, S.K., Jenkins, S.F., Vye-Brown, C., 2015. Global Volcanic Hazards and Risk. Cambridge University Press.

Maeno, F., Nakada, S., Nagai, M., Kozono, T., 2013. Ballistic ejecta and eruption condition of the vulcanian explosion of Shinmoedake volcano, Kyushu, Japan on 1 February 2011. Earth. Plan. Space 65, 609–621.

Manville, V., Németh, K., Kano, K., 2009. Source to sink: a review of three decades of progress in the understanding of volcaniclastic processes, deposits, and hazards. Sediment. Geol. 220 (3–4), 136–161.

Mastin, L., 1995. Thermodynamics of gas and steam-blast eruptions. Bulletin of Volcanology 57 (2), 85–98.

Massaro, S., Dioguardi, F., Sandri, L., Tamburello, G., Selva, J., Moune, S., Jessop, D., Moretti, R., Komorowski, J.-C., Costa, A., 2021. Testing gas dispersion modelling: a case study at La Soufrière volcano (Guadeloupe, Lesser Antilles). J. Volcanol. Geotherm. Res. https://doi.org/10.1016/j.jvolgeores.2021.107312.

Mastin, L.G., 2001. A simple calculator of ballistic trajectories for blocks ejected during volcanic eruptions. Tech. Rep.. U.S. Geol. Surv. Open-File Rep. 01–45.

Mead, S.R., Magill, C.R., 2017. Probabilistic hazard modelling of rain-triggered lahars. J. Appl. Volcanol. 6 (1), 1–7.

Mercalli, G., Silvestri, O., 1891. Le eruzioni dell'isola di Vulcano, incominciate il 3 Agosto 1888 e terminate il 22 Marzo 1890. Ann. Ufficio Centrale Meteorol. e Geodin. 10 (4), 1–213.

Moretti, R., Komorowski, J.C., Ucciani, G., Moune, S., Jessop, D., de Chabalier, J.B., Beauducel, F., Bonifacie, M., Burtin, A., Vallè, M., Deroussi, S., Robert, V., Gibert, D., Didier, T., Kitou, T., Feuillet, N., Allard, P., Tamburello, G., Shreve, T., Saurel, J.M., Lemarchand, A., Rosas-Carbajal, M., Agrinier, P., Le Friant, A., Chaudisson, M., 2020. The 2018 unrest phase at La Soufrière of Guadeloupe (French West Indies) andesitic volcano: Scrutiny of a failed but prodromal phreatic eruption. J. Volcanol. Geotherm. Res. 106769.

Orsi, G., Di Vito, M.A., Isaia, R., 2004. Volcanic hazard assessment at the restless Campi Flegrei caldera. Bull. Volcanol. 66, 514–530. https://doi.org/10.1007/s00445-003-0336-4.
Osman, S., Rossi, E., Bonadonna, C., Frischknecht, C., Andronico, D., Cioni, R., Scollo, S., 2019. Exposure-based risk assessment and emergency management associated with the fallout of large clasts at Mount Etna. Nat. Hazards Earth Syst. Sci. 19 (3), 589–610.
Pardo, N., Cronin, S.J., Nemeth, K., Brenna, M., Schipper, C.I., Breard, E., White, J.D.L., Procter, J., Stewart, B., Agustin-Flores, J., Moebis, A., Zernack, A., Kereszturi, G., Lube, G., Auer, A., Neall, V., Wallace, C., 2014. Perils in distinguishing phreatic from phreatomagmatic ash; insights into the eruption mechanisms of the 6 August 2012 Mt. Tongariro eruption. New Zealand. J. Volcanol. Geotherm. Res. 286, 397–414.
Pomonis, A., 2006. Evaluating Volcanic Risk Mitigation Measures for Buildings near Soufrière Volcano (Guadeloupe). EXPLORIS Final Report, The Martin Centre, Cambridge University Department of Architecture, Annex B.
Rosi, M., Di Traglia, F., Pistolesi, M., Ongaro, T.E., Vitturi, M.D.M., Bonadonna, C., 2018. Dynamics of shallow hydrothermal eruptions: new insights from Vulcano's Breccia di Commenda eruption. Bull. Volcanol. 80 (12), 83.
Rougier, J., Beven, K.J., 2013. Model and Data Limitations: The Sources and Implications of Epistemic Uncertainty. Risk and Uncertainty Assessment for Natural Hazards. p. 40.
Ruzié, L., Moreira, M., Crispi, O., 2012. Noble gas isotopes in hydrothermal volcanic fluids of La Soufrière volcano, Guadeloupe, Lesser Antilles arc. Chem. Geol. 304, 158–165.
Sandri, L., Thouret, J.C., Constantinescu, R., Biass, S., Tonini, R., 2014. Long-term multihazard assessment for El Misti volcano (Peru). Bull. Volcanol. 76 (2), 1–26.
Sandri, L., Costa, A., Selva, J., Tonini, R., Macedonio, G., Folch, A., Sulpizio, R., 2016. Beyond eruptive scenarios: assessing tephra fallout hazard from Neapolitan volcanoes. Sci. Rep. 6, 24271.
Scaini, C., Biass, S., Galderisi, A., Bonadonna, C., Folch, A., Smith, K., Höskuldsson, A., 2014. A multi-scale risk assessment for tephra fallout and airborne concentration from multiple Icelandic volcanoes–part 2: Vulnerability and impact. Nat. Hazards Earth Syst. Sci. 14 (8), 2289–2312.
Self, S., Wilson, L., Nairn, I., 1979. Vulcanian eruption mechanisms. Nature 277, 440–443.
Selva, J., Costa, A., Sandri, L., Marzocchi, W., 2010. BET_VH: exploring the influence of natural uncertainties on long-term hazard from tephra fallout at Campi Flegrei (Italy). Bull. Volcanol. 72, 717–733.
Selva, J., Orsi, G., Di Vito, M.A., Marzocchi, W., Sandri, L., 2012. Probability hazard map for future vent opening at the Campi Flegrei caldera. Italy. Bull. Volcanol. 74 (2), 497–510.
Selva, J., Costa, A., De Natale, G., Di Vito, M.A., Isaia, R., Macedonio, G., 2018. Sensitivity test and ensemble hazard assessment for tephra fallout at Campi Flegrei. Italy. J. Volcanol. Geotherm. Res. 351, 1–28.
Selva, J., Bonadonna, C., Branca, S., De Astis, G., Gambino, S., Paonita, A., Pistolesi, M., Ricci, T., Sulpizio, R., Tibaldi, A., Ricciardi, A., 2020. Multiple hazards and paths to eruptions: a review of the volcanic system of Vulcano (Aeolian Islands, Italy). Earth Sci. Rev. 207, 103186. https://doi.org/10.1016/j.earscirev.2020.103186.
Sheridan, M.F., 1980. Pyroclastic block flow from the September, 1976, eruption of La Soufrière volcano. Guadeloupe. Bull. Volcanol. 43, o397–o402.
Sheridan, M.F., Malin, M.C., 1983. Application of computer-assisted map- ping to volcanic hazard evaluation of surge eruptions: Vulcano, Lipari, and Vesuvius. J. Volcanol. Geotherm. Res. 17 (1–4), 187–202.
Siebert, L., Simkin, T., 2002–2011. Volcanoes of the World: an Illustrated catalog of Holocene Volcanoes and their Eruptions. Smithsonian Institution, Global Volcanism Program Digital Information Series, GVP-3 http://www.volcano.si.edu Accessed 17 July 2013.
Sobradelo, R., Martí, J., 2010. Bayesian event tree for long-term volcanic hazard assessment: Application to Teide-Pico Viejo stratovolcanoes, Tenerife, Canary Islands. J. Geophys. Res. Solid Earth 115 (B5).
Spence, R.J.S., Kelman, I., Baxter, P.J., Zuccaro, G., Petrazuolli, S., 2005. Residential building and occupant vulnerability to tephra fall. Nat. Hazards Earth Syst. Sci. 5, 477–494.
Spence, R., Komorowski, J.C., Saito, K., Brown, A., Pomonis, A., Toyos, G., Baxter, P., 2008. Modelling the impact of a hypothetical sub-Plinian eruption at La Soufrière of Guadeloupe (Lesser Antilles). J. Volcanol. Geotherm. Res. 178 (3), 516–528.
Sulpizio, R., Zanchetta, G., Caron, B., Dellino, P., Mele, D., Giaccio, B., Insinga, D., Paterne, M., Siani, G., Costa, A., Macedonio, G., Santacroce, R., 2014. Volcanic ash hazard in the Central Mediterranean assessed from geological data. Bull. Volcanol. 76 (10), 866.
Sword-Daniels, V., 2011. Living with volcanic risk: the consequences of, and response to, ongoing volcanic ashfall from a social infrastructure systems perspective on Montserrat. New Zealand J. Psyc. 40, 131–138.
Taddeucci, J., Alatorre-Ibargüengoitia, M.A., Cruz-Vázquez, O., Del Bello, E., Scarlato, P., Ricci, T., 2017. In-flight dynamics of volcanic ballistic projectiles. Rev. Geophys. 55 (3), 675–718.
Tadini, A., Bevilacqua, A., Neri, A., Cioni, R., Aspinall, W.P., Bisson, M., Isaia, R., Mazzarini, G.A., Valentine, S., Vitale, P., Bacter, A., Bertagnini, M., Cerminara, M., de Michieli Vitturi, M., Di Roberto, S., Ewgwell, T., Esposti-Ongaro, T., Flandoli, F., Pistolesi, M., 2017. Assessing future vent opening locations at the Somma-Vesuvio volcanic complex: 2. Probability maps of the caldera for a future Plinian/sub-Plinian event with uncertainty quantification. J. Geophys. Res. Solid Earth 122 (6), 4357–4376.
Tamburello, G., Moune, S., Allard, P., Venugopal, S., Robert, V., Rosas-Carbajal, M., Deroussi, Gaëtan-Thierry Kitou, Didier, T., Komorowski, J.C., Beauducel, F., De Chabalier, J.B., Le Marchand, A., Le Friant, A., Bonifacie, M., Dessert, C., Moretti, R., 2019. Spatio-Temporal Relationships between Fumarolic activity, Hydrothermal Fluid Circulation and Geophysical Signals at an Arc Volcano in Degassing Unrest: La Soufrière of Guadeloupe (French West Indies). Geosciences 9 (11), 480.
Thompson, M.A., Lindsay, J.M., Sandri, L., Biass, S., Bonadonna, C., Jolly, G., Marzocchi, W., 2015. Exploring the influence of vent location and eruption style on tephra fall hazard from the Okataina Volcanic Centre. New Zealand. Bull. Volcanol. 77 (5), 1–23.
Tierz, P., Sandri, L., Costa, A., Sulpizio, R., Zaccarelli, L., Di Vito, M.A., Marzocchi, W., 2016. Uncertainty Assessment of Pyroclastic Density Currents at Mount Vesuvius (Italy) Simulated through the Energy Cone Model. In K. Riley, P. Webley, and M. Thompson (Eds) "Natural Hazard Uncertainty Assessment: Modeling and Decision Support". Geophysical Monograph 223. I edition. Am. Geophys. Union, John Wiley & Sons, Inc.
Tilling, R.I., 1989. Volcanic hazards. Am. Geophys. Union vol. 1.
Tsunematsu, K., Ishimine, Y., Kaneko, T., Yoshimoto, M., Fujii, T., Yamaoka, K., 2016. Estimation of ballistic block landing energy during 2014 Mount Ontake eruption. Earth, Plan. Space 68 (1), 1–11.
Vanderkluysen, L., Harris, A., Kelfoun, K., Bonadonna, C., Ripepe, M., 2012. Bombs behaving badly: unexpected trajectories and cooling of volcanic projectiles. Bull. Volcanol. 74, 1849–1858.
Villemant, B., Hammouya, G., Michel, A., Semet, M.P., Komorowski, J.C., Boudon, G., Cheminée, J.L., 2005. The memory of volcanic waters: shallow magma degassing revealed by halogen monitoring in thermal springs of La Soufrière volcano (Guadeloupe, Lesser Antilles). Earth Planet. Sci. Lett. 237 (3–4), 710–728.
Villemant, B., Komorowski, J.C., Dessert, C., Michel, A., Crispi, O., Hammouya, G., De Chabalier, J.B., 2014. Evidence for a new shallow magma intrusion at La Soufrière of Guadeloupe (Lesser Antilles): insights from long-term geochemical monitoring of halogen-rich hydrothermal fluids. J. Volcanol. Geotherm. Res. 285, 247–277.
Wardman, J.B., Wilson, T.M., Bodger, P.S., Cole, J.W., Stewart, C., 2012. Potential impacts from tephra fall to electric power systems: a review and mitigation strategies. Bull. Volcanol. 74-2221, 2241.
Williams, G.T., Kennedy, B.M., Wilson, T.M., Fitzgerald, R.H., Tsunematsu, K., Teissier, A., 2017. Buildings vs. ballistics: Quantifying the vulnerability of buildings to volcanic ballistic impacts using field studies and pneumatic cannon experiments. J. Volcanol. Geotherm. Res. 343, 171–180.
Wilson, T.M., Stewart, C., Sword-Daniels, V., Leonard, G.S., Johnston, D.M., Cole, J.W., Wardman, J.B., Wilson, G., Barnard, S.T., 2012. Volcanic ash impacts on critical infrastructure. Phys. Chem. Earth 45–46, 5–23.
Wilson, G., Wilson, T., Deligne, N.I., Cole, J.W., 2014. Volcanic hazard impacts to critical infrastructure: a review. J. Volcanol. Geotherm. Res. 286-148, 82.
Wilson, G., Wilson, T.M., Deligne, N.I., Blake, D.M., Cole, J.W., 2017. Framework for developing volcanic fragility and vulnerability functions for critical infrastructure. J. Appl. Volcanol. 6, 14. https://doi.org/10.1186/s13617-017-0065-6.